PCCP

Accepted Manuscript

ROYAL SOCIETY OF CHEMISTRY

www.rsc.org/pccp

Understanding the Role of Iron in the Magnetism of Fe-Doped ZnO Nanoparticles

J.J. Beltrán[1, 2], C. A. Barrero[1] and A. Punnoose[2]

[1]*Grupo de Estado Sólido, Facultad de Ciencias Exactas y Naturales, Universidad de Antioquia UdeA, Calle 70 No 52-21, Medellín, Colombia.*

[2] *Department of Physics, Boise State University, Boise, Idaho 83725-1570, USA.*

ABSTRACT: The actual role of transition metals like iron in the room temperature ferromagnetism (RTFM) of Fe doped ZnO nanoparticles is still an unsolved question. While some studies concluded that the Fe ions participate in the magnetic interaction, others on the contrary do not believe Fe as playing a direct role in the magnetic exchange interaction. To contribute to the understanding of this issue, we have carefully investigated the structural, optical, vibrational and magnetic properties of Sol-Gel synthesized $Zn_{1-x}Fe_xO$ ($0<x<0.10$) nanoparticles. No Fe^{2+} was detected in any sample. We found that high spin Fe^{3+} ions are substitutionally incorporated at the Zn^{2+} in the tetrahedral-core sites and in pseudo-octahedral surface sites in ZnO. Superficial OH^- was observed in all samples. For $x \leq 0.03$, increment in Fe doping concentration decreased a and c lattice parameters, average Zn-O bond length, average crystallite size and band gap; while it increased degree distortion and quadrupole splitting. Undoped ZnO nanoparticles exhibited very weak RTFM with saturation magnetization (M_s) of ~ 0.47 memu/g and this value increased to ~2.1 memu/g for $Zn_{0.99}Fe_{0.01}O$. Very interestingly, the M_s for $Zn_{0.99}Fe_{0.01}O$ and $Zn_{0.97}Fe_{0.03}O$ increased by a factor of about ~2.3 by increasing annealing from 1 h to 3. For $x \geq 0.05$ ferrimagnetic disordered spinel $ZnFe_2O_4$ was formed and this phase was found to become more ordered with increasing annealing time. Fe does not contribute directly to the RTFM, but its presence promoted the formation of additional single charged oxygen vacancies, zinc vacancies, and more oxygen-ended polar terminations at the nanoparticle surface. These defects, which are mainly superficial, altered the electronic structure and are considered as the main sources of the observed magnetism.

Keywords: Optical Absorption; Mössbauer spectroscopy; Room temperature ferromagnetism; Defects. ** Corresponding Author E-mail: jjbj08@gmail.com*

1. INTRODUCTION

Transition metal (TM) doped ZnO have been extensively studied since the prediction by Dietl *et.al* that doping Mn into the nonmagnetic ZnO host could induce ferromagnetic (FM) behavior at room temperature (RT) in this semiconducting material.[1] In the TM doped ZnO system, the role of Fe ions have been widely explored both theoretically and experimentally. However, there are several issues that remain unclear and require more detailed investigations, among them the maximum solubility limit of iron in ZnO lattice, the direct or indirect participation of Fe in the RTFM signal, the actual oxidation state of iron (Fe^{2+}, Fe^{3+} or the combination of both), and the appropriate magnetic model to explain the origin of the RTFM. Regarding the maximum solubility limit of iron, it remains imprecise, but has been shown, in most of the reports that this limit lies in the range of 3 to 8 at. %.[2–8] At higher Fe concentrations, $ZnFe_2O_4$ has been reported as the primary spurious phase. The contribution of this impurity phase to the magnetism in Fe doped ZnO is also controversial. Bulk ordered $ZnFe_2O_4$ has normal spinel structure where Zn^{2+} and Fe^{3+} cations occupy tetrahedral and octahedral sites respectively, and is normally antiferromagnetic (AFM) at RT. However, in the disordered state for which Zn^{2+} and Fe^{3+} are distributed amongst both sites, an effective ferrimagnetic (FiM) ordering can appear.[9,10] In this case the chemical formula is $(Zn_{1-x}Fe_x)[Fe_{2-x}Zn_x]O_4$, where round and square brackets denote sites of tetrahedral (A) and octahedral [B] coordinations, respectively, and where x represents the inversion parameter and corresponds to the degree of cation distribution. Shim *et al.* have reported that the ferromagnetism in Fe-Cu co-doped ZnO, prepared by solid state reaction method, comes from $ZnFe_2O_4$ FiM nanocluster impurities with inverted spinel structure.[11] Mandal *et al.* [12] found that in $Zn_{1-x}TM_xO$ (TM=Co, Mn, Fe, and Ni), the solubility limit of TM depends on both growth temperature and doping concentration. The evolution of secondary phases reduces the magnetization in all cases and seemingly may not be the source of the observed magnetic properties of ZnO based in dilute magnetic semiconductor (DMS). Similarly, it was also found that the magnetization of Fe doped ZnO starts to decrease on further doping while the amount of $ZnFe_2O_4$ spinel structure increases.[13] These two latter reports suggest that the ferromagnetism in TM doped ZnO system is an intrinsic property mainly because this spurious spinel phase is AFM. From these studies, it is evident that a clear distinction between ordered and disordered $ZnFe_2O_4$ phase is required in order to discern if the magnetism of Fe doped ZnO is truly intrinsic or if it originates from that of the impurity phase.

Another interesting controversy is about the actual oxidation state of Fe in ZnO. First-principle theoretical studies have been performed assuming only Fe^{2+} in defect-free ZnO, Fe^{2+} and Fe^{3+} in the presence of Zn and O vacancies or both oxidation states.[14–16] Now, regarding experimental works, there is evidence from ^{57}Fe Mössbauer, NEXAFS or XPS measurements that Fe atoms occupy the host ZnO lattice in two distinct states Fe^{2+} and Fe^{3+},[7,13,16–18] however other studies have observed Fe^{3+} ions only.[19–22] This may be due to differences in the preparation conditions of the samples, such as precursors, reactants, reaction/processing temperature, pH etc. In fact, it is well known that the method employed to prepare this system (mechanical alloying,[23,24] solid state reaction method[25,26], and wet chemistry methods) can determine the physico-chemical, crystallographic and magnetic properties of the final product. Moreover, even when using similar preparation methods and same nominal concentrations, the magnetic properties are sometimes not reproducible.

The direct or indirect participation of Fe in the RTFM signal is another unsolved problem. Most studies have concluded that the Fe ions directly participate in the magnetic interaction,[13,21,27,28] however others on the contrary claimed that Fe does not directly participate.[16,22] Thus, the origin of the observed RTFM in Fe doped ZnO is highly controversial and several models have been proposed for explain it, such as: super-exchange interaction between Fe ions, interaction between magnetic polarons, spin split impurity band, metamagnetism, charge transfer ferromagnetism, small magnetic dipoles located at the surface of nanocrystals which interacts with their nearest neighbors inside the crystal, or that defects may be mainly responsible for getting the FM order among others.

In this respect, in our previous reports, we have prepared Fe doped Co doped and Fe and Co codoped ZnO by using a Sol Gel method.[29,30] Those studies suggested that the simultaneous introduction of Fe and Co ions in the ZnO lattice has a strong synergistic effect, because they eliminated the formation of the $ZnFe_2O_4$ impurity phases and produced much stronger FM signal in comparison to that observed in ZnO doped with only one of the cations.[29] But, the most important finding was that the saturation magnetization (*Ms*) did not depend on the magnetic interactions involving Co^{2+} or Fe^{3+}; instead, M_s and Co^{3+} concentration increased systematically with increase in the codoping concentration. The magnetic signal was not related to the magnetic moments of the TM ions, but was interpreted in terms of the charge transfer ferromagnetism involving mixed valence ions, most likely Co^{3+} and Co^{2+}, in addition to changes in the electronic structure associated with the presence of extended defects in the nanoparticles[30]. These results raised the question about the real role of iron in the magnetism of this codoped system and of Fe doped ZnO.

In this work, we carefully characterize the crystallographic, vibrational, optical and magnetic properties of $Zn_{1-x}Fe_xO$ ($0<x<0.10$) nanoparticles prepared by a Sol-Gel method. The main goals are to: (i) provide information about the solubility limit of Fe dopant ions in ZnO lattice, (ii) discern the magnetism originated from $ZnFe_2O_4$ and that from Fe-doped ZnO, (iii) search for the actual oxidation state (Fe^{3+} or Fe^{2+}) and discern the participation of Fe in the RTFM signal, (iv) infer about the preferred location of the Fe ions in the ZnO lattice, and (v) to contribute to the understanding of the role of iron ions on the magnetic properties of Fe doped ZnO.

2. EXPERIMENTAL DETAILS

Nanocrystalline $Zn_{1-x}Fe_xO$ ($0.0 \leq x \leq 0.10$) powders were prepared by the citrate precursor method based on the modified Pechini process.[31] $Zn(NO_3)_2\cdot 6H_2O$, $Fe(NO_3)_3\cdot 9H_2O$, citric acid (CA), ethylene glycol (EG), 5M ammonia solution and deionized water were used for the preparation of the starting sol. First the metal nitrates, in required molar ratios, and CA were dissolved in 200 mL of deionized water with a {[Zn]+[Fe]}:/[CA] molar ratio of 1:3.The resultant sol was heated at 70 °C under constant stirring and the pH of the solution was adjusted to 5 by adding ammonia solution dropwise. Then, EG with EG/CA ratio of 5 was added to the mixture. Thus, the combination of EG and CA may result in more stable chelate complex. The solution temperature was increased and kept between 90 and 95 °C for ~ 4h, to evaporate water. Finally, the temperature was raised slowly between 100 and 110 °C, to promote the polysterification and the system was maintained until the bar stirring stopped by itself. In this last step the solution became more viscous and finally turned into wet gel. The wet gel thus formed was dried at 200 °C in air for 4 h to get rid of volatile components, resulting in a black solid mass. These black powder precursors were annealed in a tubular furnace at 550 °C (heating rate: 5 °C/min) in air atmosphere for 1 h and 3 h. To obtain more insight into possible Fe impurity phases which might be formed under these synthesis conditions, $ZnFe_2O_4$ was also prepared following identical synthesis procedures. These fine powders of the as-obtained product were characterized by X ray diffraction, Fourier transform infrared spectroscopy, optical absorption measurements, RT ^{57}Fe Mössbauer spectroscopy and variable temperature magnetic measurements.

X-ray diffraction (XRD) patterns were collected at RT using a Phillips X'Pert X-ray diffractometer with Cu-Kα source (λ= 1.5406Å) in Bragg-Brentano geometry. The XRD patterns were fitted using the Rietveld method to obtain crystalline cell parameters. Fourier transform infrared (FTIR) spectra of the samples were recorded using FTIR Bruker tensor 27 Spectrophotometer, using the KBr pellet technique, with an experimental resolution of 4 cm^{-1} approximately. RT optical absorption spectra in the ultraviolet and visible light wavelength were measured using an Evolution 600 UV–Vis spectrophotometer (Thermo Scientific) fitted with an integrating sphere diffuse reflectance accessory. ^{57}Fe Mössbauer spectra were recorded at RT using a conventional Mössbauer spectrometer working in the transmission geometry and using a drive with triangular reference signal at constant acceleration. The ^{57}Fe Mössbauer spectra were calibrated using 7 µm thick α- ^{57}Fe foil as standard absorber at 300 K. The data were fitted with Lorentzian line shapes. The magnetic properties of the samples were studied using a PPMS -Physical Property Measurement System-, Model 6000 (Quantum Design, San Diego, CA.) equipped with a superconducting magnet. The Magnetic measurements were carried out as a function of applied magnetic field of ±0.5 T and as a function of temperature (5-300 K).

3. RESULTS

3.1 *X-ray Diffraction*: Typical refined patterns using the Rietveld method for $Zn_{1-x}Fe_xO$ ($0.0 \leq x \leq 0.10$) nanoparticles annealed at 550 °C for 1 h, along with $ZnFe_2O_4$ sample prepared as reference are depicted in Figure 1. Only pure wurtzite phase of ZnO, without any evidence of impurity or secondary crystalline phases, was obtained for $Zn_{1-x}Fe_xO$ samples (with $0.0 \leq x \leq 0.05$) within the sensitivity of the technique. However, small peaks corresponding to cubic $ZnFe_2O_4$ were observed in the patterns of $Zn_{0.92}Fe_{0.08}O$ (1.8 wt. %) and $Zn_{0.90}Fe_{0.10}O$ (2.7 wt. %) indicated by the orange vertical bars in the fit. These peaks are more evident when XRD patterns are plotted in logarithmic scale (see arrows top panel at the right side of the Figure 1). Signals corresponding to α-Fe, α-Fe_2O_3, γ-Fe_2O_3 or Fe_3O_4 were not detected in any of the samples. With increasing iron concentration x, a systematic increase in the full width at half maximum (FWHM) and decrease in the intensity of the diffraction peaks of ZnO were observed. These changes indicate that with increasing Fe doping there is a reduction in the average crystallite size (Dv) and a loss in crystallinity of the wurzite ZnO phase. These results suggest that Fe in ZnO structure inhibits crystallite growth, perhaps by modifying the rate of nucleation during the ZnO crystallization. The a and c lattice parameters of ZnO along with the average Zn–O bond length (L) parallel to the c-axis[32] and the crystal lattice distortion degree (R)[33] as a function of Fe content for all samples are displayed in Figure 2. As the Fe concentration increase up to 5 %, the a and c lattice parameters decrease and then increase upon further doping, while parameter L follow the same trend [see Fig 2(a) and (b)]. It is worth mentioning that Ahmed *et al.* have found a completely opposite trend in Fe doped ZnO nanostructures when the Fe content in ZnO lattice reaches up to 5 % doping.[13] In an ideal stoichiometric wurtzite structure the c/a

ratio is 1.633.[32] Our undoped as well as Fe doped samples showed significantly smaller *c*/*a* ratio in the range of 1.6008-1.6026, which might indicate the presence of oxygen vacancies, zinc vacancies.[32] In comparison to *x*= 0, all Fe doped ZnO samples have smaller *c*/*a* and *L* and higher *R* values at higher Fe content. Furthermore, the *R* parameter increases until *x*= 0.03 and beyond this nominal percentage a definite trend is not observed [see Figure 2(c)]. In a tetrahedral environment and high spin state, the ionic radii of Fe^{3+} (discussed elsewhere in this work using Mössbauer spectroscopy) and Zn^{2+} are 0.49 and 0.60 Å, respectively.[34] Therefore, a decrease in the lattice parameter is expected as Fe concentration increases for a $Zn_{1-x}Fe_xO$ solid solution. These results indicate that, within the detection limit of XRD, Fe ions may be substituting for Zn in the wurzite lattice up to 5 % doping, under the present synthesis conditions. Doping of Fe above $x = 0.05$ might lead to co-existence of the dominant phase $Zn_{1-x}Fe_xO$ and along with weak spinel phase $ZnFe_2O_4$.

On the other hand, the XRD patterns of $Zn_{1-x}Fe_xO$ ($0.0 \leq x \leq 0.10$) nanoparticles annealed for 3 h, with the same Fe nominal concentration, showed higher *a* and *c* lattice parameters, better crystallinity and slightly higher *Dv* values in comparison to those samples annealed for 1 h (data not shown). In this case, the *a* and *c* lattice parameters suggest that the solubility limit in this set of samples is lower than 5 % doping. To obtain more insight about the purity of 3% Fe doped ZnO sample annealed for 3 h, we have recorded XRD pattern for this sample enhancing the detection limit considerably. This pattern plotted in logarithmic scale (data not shown) did not reveal any phase other than ZnO.

3.2 ***Fourier transformed infrared spectroscopy***: Figure 3 shows the FTIR spectra in the wavenumber range of 400-4000 cm^{-1} for $Zn_{1-x}Fe_xO$ with x =0, 0.01, 0.03 and 0.05 annealed for 1 h. The intense band centered at around 470 cm^{-1} is assigned to antisymmetric stretching vibration of O-Zn–O bonds, which also confirms the wurtzite structure.[35] All spectra exhibit two very weak peaks located at ~2850 and 2925 cm^{-1} due to C-H bond bending and stretching, respectively and two weak bands at 1390 and 1630 cm^{-1} attributed to the antisymmetric and symmetric C=O stretching modes, commonly associated with the carboxylate functional group, possibly originating from the fragments of the citrate precursor. It is worth mentioning that these bands are not considered as contamination of the nanoparticles, rather they point out to the presence of absorbed species on the surface of nanopowders that could influence the properties of ZnO that depends primarily on the surface structure.[36] The intense and broad absorption in the range of 3100-3700 cm^{-1} is due to the stretching vibration of hydroxyl groups attached on the surface of nanocrystalline powders, indicating the existence of water absorbed on the surface of ZnO grains. This possibly could be attributed to the polarity of ZnO. Water dissociation often is favored at ZnO oxide surfaces, leaving OH^- groups and hydrogen ions (H^+) ions, where the stacking of Zn^{2+} ions (0001) plane tends to bind the hydroxide and the stacking of O^{2-} $(000\bar{1})$ plane ions tends to under-coordinated with the hydrogen, due to the electrostatically instability of these planes.[37] On the other hand, the FTIR spectra of $Zn_{1-x}Fe_xO$ ($0.0 \leq x \leq 0.05$) nanoparticles annealed for 3 h showed vibrational absorption bands very similar to those presented in Figure 3 (data not shown).

3.3 *Optical absorption*: RT optical absorption spectra of ZnO and Fe doped ZnO nanoparticles (with different Fe concentrations) annealed at 550 °C for 1 h is shown in Figure 4a. The spectrum of $ZnFe_2O_4$ is also included as reference. In the spectra of the Fe doped ZnO samples with $x = 0.01$, 0.03 and 0.05 a small shoulder in the region from 460 to 490 nm (rectangular area) is observed. This weak hump is interpreted as *d-d* crystal-field transitions between multiplets of $3d^5$ configuration of the high spin Fe^{3+} substituting for Zn^{2+} under the influence of a tetrahedral crystal field.[38] These are ascribed as transitions from $^6A_{1g}$ ground states to $^4T_1$, $^4T_2{}^4E$, and $^4A_1$ excited states. The first excited ^4G state of free d^5 ion is split into $^4T_1$, $^4T_2{}^4E$, and $^4A_1$ in the order of increasing energy under a *Td* crystal field. Similar transitions are also observed in Fe doped ZnO nanocrystal[27] and for Mn^{2+} doped ZnO, where the $3d^5$ ion is isoelectronic with Fe^{3+}.[39] On the other hand, for the highest Fe doped samples, *i.e.*, $x= 0.08$ and 0.10, this band is located in a position similar to that of the $ZnFe_2O_4$ sample (encircled area) and a weak shoulder located around 420 nm appears (shown by the dash arrow in Figure 4a). This peak may be related to the presence of a weak impurity phase of $ZnFe_2O_4$, as observed in XRD data also. According to XRD and optical absorption results the solubility limit in these Fe doped ZnO samples is about 5%. From the derivative of the optical absorption curves, (see Figure 4b) the strong absorption peak centered at ~380 nm, which arises from ZnO at the band edge, was observed to shift towards lower wavelengths (~375 nm for $x = 0.10$) and to decrease in intensity with increasing Fe concentration. This trend could also be an evidence of the substitution of Fe^{3+} ions in ZnO structure and indicate that this dopant act as donor.[27] These observations clearly demonstrate that the electronic structure has been altered by the iron doping. Additionally, the presence of $ZnFe_2O_4$ phase in $Zn_{1-x}Fe_xO$ samples with $x = 0.08$ and 0.10 was clearly evidenced.

The inset of Figure 4a shows the variation of the band gap (*Eg*), obtained following the Kubelka-Munk equation, and the average crystallite size (*Dv*), obtained by Rietveld analysis of the XRD patterns, with the nominal Fe content. The $ZnFe_2O_4$ sample gave a *Eg* value of 2.05 eV, which is lower than that observed in all the Fe doped ZnO samples. The low *Eg* (=3.23 eV) for the undoped ZnO nanoparticles compared to that of the bulk (=3.37 eV), might be due to the presence of oxygen and/or zinc vacancies, other defects at the particles surface or nanometric size effect.[41] One can notice a gradual decrease of *Eg* and *Dv* with increasing Fe content in the samples. These results are in close agreement with that reported earlier by other groups.[18,42,43] Saleh *et al.* have reported that the band gap energy decreases with an increase in the lattice parameters of ZnO structure with increasing Fe concentrations.[18] Anghel *et al.* observed that changes in band gap were very similar to the observed changes in the unit cell volume with increasing Fe content.[44] In our case, according to XRD results, the change in the band gap cannot be explained on the basis of the variation of the lattice parameters observed in the Fe doped ZnO samples. From the inset of Figure 4a correlation between *Eg* and *Dv* is clearly evidenced, regardless the presence of $ZnFe_2O_4$ phase. The average crystallite sizes of these Fe doped ZnO nanoparticles ($\geq$ 14 nm) are much larger than the exciton Bohr radius of ZnO (~1.8 nm)[45] for which quantum confinement effect becomes important. So this effect is not a major player in the band gap of these samples. This gradual decrease in the band gap with increasing x may be mainly related to the stronger exchange interactions between the localized d electrons of the Fe ions substituting for Zn^{2+} ions and the s and p electrons of the host band of ZnO, leading to a negative and a positive correction to the conduction band and the valence band edges, respectively, resulting in a band gap narrowing.[42] Another explanation could be related to the enhanced band bending at grain boundaries. Samples with lower grain size have higher grain surface area, causing more band bending effect as reported by Dutta *et al.*[41] On the other hand, the RT optical absorption spectra of $Zn_{1-x}Fe_xO$ ($0.0 \leq x \leq 0.10$) nanoparticles annealed for 3 h (data not shown) are very similar to the curves presented in Figure 4a. Band gap values of 3.22, 3.19, 3.17, 3.15, 3.06 and 3.0 eV for $x = 0$, 0.01, 0.03, 0.05, 0.08, and 0.10 respectively, were obtained. It is noted that these band gap values are smaller than those for the samples annealed for 1 h, although the latter samples have smaller crystallite sizes compared to the former ones (3 h annealed samples). These results can be due to the fact that the structural changes, caused by the dopant incorporation and the prolonged annealing time, have a dominant role in the observed changes of the band gap. Drastic changes in the band gap of x=0.05 to 0.08 can be ascribed to the additional contribution of $ZnFe_2O_4$ impurity phase.

3.4 *RT ^{57}Fe Mössbauer spectroscopy*: Figure 5 displays the RT ^{57}Fe Mössbauer spectra of $Zn_{1-x}Fe_xO$ ($x = 0.01$, 0.03, 0.05, 0.08, and 0.10) nanopowders annealed at 550 ^{o}C for 1 h along with the spectrum of $ZnFe_2O_4$ prepared as reference. The derived hyperfine parameters for these samples are gathered in Table I. The spectrum of $ZnFe_2O_4$ displays a well-defined doublet whose hyperfine parameters are in good agreement with those reported in literature for nanosized material.[46] All Mössbauer spectra of Fe doped ZnO samples consisted of only doublets and no magnetic hyperfine pattern (sextets) could be observed within the detection limit of the technique, suggesting that presence of magnetic impurities phases such as metallic iron, α-Fe_2O_3, γ-Fe_2O_3 or Fe_3O_4 iron oxides can be ruled out. Additionally, this observation suggests that at RT the Fe ions in ZnO structure do not order magnetically. To analyze the observed Mössbauer spectra of both $Zn_{0.99}Fe_{0.01}O$ and

$Zn_{0.97}Fe_{0.03}O$ samples, a model including two doublets, doublet 1 (D1) and doublet 2 (D2), was necessary. The hyperfine parameters of these doublets (see Table I), suggest that there are two kinds of Fe ions, both in high spin 3+ sites, but located in different chemical environments. Similar RT ^{57}Fe Mössbauer results were observed by Limaye *et al*. in Fe doped ZnO nanorods[21] and Carvalho *et al.* in Fe doped ZnO powders prepared by self-combustion method.[19] Carvalho *et al.* have associated this second doublet to Fe^{3+} ions in different vicinities replacing Zn^{2+} ions, which tend to compensate defects, such as cation vacancies, to maintain charge neutrality. Apart of these two doublets, in Fe doped ZnO samples with $x = 0.05$, 0.08 and 0.10, the necessity of a third doublet (D3) is evident due to presence of a small shoulder located at the central part of the spectrum, markedly improving the fitting. The hyperfine parameters of this doublet show isomer shifts, δ, in the range of $0.32\ \text{mm/s} < \delta < 0.34\ \text{mm/s}$ and quadrupole splittings, Δ, in the range of $0.37\ \text{mm/s} < \Delta < 0.40\ \text{mm/s}$, (see Table 1) which match well with the hyperfine parameters of $ZnFe_2O_4$. Moreover, the relative area of D3 increases with increasing Fe content, suggesting increasing presence of $ZnFe_2O_4$ in the higher Fe doped samples. These results indicate that Mössbauer spectroscopy is a very sensible tool and a powerful local probe technique to detect impurity phases in these Fe doped ZnO samples due to that the detection of $ZnFe_2O_4$ phase which completely escaped detection in the XRD pattern of $Zn_{0.95}Fe_{0.05}O$ sample, even when plotted in logarithmic scale and also of optical absorption spectroscopy. It is worth mentioning that no signature of Fe^{2+} has been found in any of these spectra. Similar results have been reported by some researchers,[19,21,22,28,47] where only the presence of Fe^{3+} is detected and not Fe^{2+}. From the analysis of the Mössbauer spectra, it was also found that D1 and D2 showed isomer shifts, δ, in the range of $0.25\text{mm/s} < \delta <$

0.30 mm/s, which match well with Fe^{3+} replacing Zn^{2+} in tetrahedral sites of 4 fold coordination *i.e.* $^{[4]}Fe^{3+}$.[48] On the other hand, D1 showed quadrupole splittings, Δ, in the range of 0.73 mm/s < Δ < 0.91 mm/s while D2 showed much higher values in the range of 1.18 mm/s<Δ< 1.53 mm/s, suggesting that the Fe^{3+} ions replacing Zn^{2+} ions in different locations of the ZnO nanoparticles. Based on these data we attribute this D1 doublet to Fe^{3+} ions, in less distorted tetrahedral sites, far from defects, more probably in the core of ZnO nanoparticles, while D2 is assigned to Fe^{3+} ions replacing Zn^{2+} in more distorted tetrahedral sites *i.e.* Fe^{3+}close to oxygen and/or zinc vacancies/ defective sites or bound to –OH groups, presumably in the surface region, where the probability of the presence of vacancies is higher.[16] From Table I it is noticed that the relative area of D2 remains reasonably constant with varying Fe concentration. On the contrary, the area of D1 decreases at the expense of D3 as Fe content increases. The Mössbauer spectrum of $Zn_{0.97}Fe_{0.03}O$ annealed for 3 h (data not shown) was similar to the previous ones and the presence of $ZnFe_2O_4$ impurity phase was not detected. It worth mentioning that the relative area (28 %) and Δ D2 (1.34 mm/s) were higher than the sample with same nominal concentration, but annealed for 1h, indicating more Fe^{3+} close to defective sites (oxygen and/or zinc vacancies). Figure 6 shows the variation of the Δ D2 and lattice volume (*V*) with nominal Fe concentration. For these Fe doped ZnO nanoparticles annealed for 1h, it is observed that Δ varies inversely with *V,* displaying a higher Δ D2 and lower *V* at 5 at. %. This gradual increase in Δ D2, could be explained by lattice relaxation effect due to the incorporation of Fe ions in ZnO structure, bringing about higher distortion with increasing Fe content. The decrease of Δ with further Fe doping might be related to the increasing presence of $ZnFe_2O_4$ in surface region. Larger Δ D2 in $Zn_{0.95}Fe_{0.05}O$ in comparison to $Zn_{0.97}Fe_{0.03}O$ sample might indicate a wider distribution of more distorted Fe^{3+} sites and that oxygen vacancies/defects are more dominant in comparison to $ZnFe_2O_4$ phase, leading to redistribution of the charges around.

3.5 *Magnetic measurements*: In order to better understand the effect of Fe on the magnetic properties of Fe doped ZnO, it is important to first investigate if undoped pure ZnO exhibits magnetism. Figure 7a shows the RT M vs H curve of ZnO nanoparticles, after subtracting the diamagnetic background contribution. This sample exhibit very weak RT ferromagnetism (RTFM) with saturation magnetization (M_s) of about 0.47 memu/g. Previous works have also reported RTFM in capped ZnO nanoparticles,[49,50] in ZnO exhibiting different morphologies[51–54] and also in uncapped ZnO nanoparticles.[55] Inset of Figure 7a shows zero-field-cooled (ZFC) and field-cooled (FC) curves for this sample. The splitting between these curves is also an indication of the FM signal. Similar behavior in these curves has been observed by Limaye *et al.*[21] RT EPR spectra of pure ZnO sample exhibits a broad signal at 3117 G (g ~2.15) which is related to ferromagnetic resonance (FMR) (see Figure 7b). This result is in good agreement with that reported by Limaye *et al.*[21] and Motaung *et al.*[54] Moreover, a weak sharp single line with line width of about 8 Oe and with $g \sim 2.004$ (3352 G) appears (see inset of Figure 7b). When a hole is involved as lattice defect, the EPR signal from zinc vacancy (V_{Zn}) defect centers should have a g-factor larger than the one due to the free electron, i.e. $g > 2.0023$[56], and then it can be assigned to a singly V_{Zn}. On the other hand, the single charged oxygen vacancies (V_O^+) at the ZnO surfaces are stable and could also account for the EPR signal at $g \sim 2.00$.[55] Therefore, the $g \sim 2.004$ signal can arises from core defects and surface or near surface defects (core shell model) as reported by Jakes and Erdem[57] and Parashar *et al.*[56], where V_{Zn} and V_O^+ being the most probable defects.

In order to check if the RTFM probably originates from traces of some other metal impurities, we performed some XPS and EDX analysis of the ZnO nanoparticles. By taking closer inspection of the survey XPS, traces of TM were not detected as is shown in Figure 7c. Similar results were obtained in EDX analysis also, for which we have chosen randomly two different points in the sample and about the same zinc and oxygen concentration were observed for all samples (data not shown). Additionally, high resolution XPS scans of Mn, Fe, Co and Ni 3p region (see inset in Figure 7c) further ruled out the presence of these ions. It is worth mentioning that high resolution scan of the Fe 2p region in undoped ZnO, revealed only a strong band at ~717.5 eV, which was associated to the Auger peak of Zn (data not shown). High resolution XPS scans of the O 1s core electron regions of the undoped ZnO sample is displayed in Figure 7d. This signal was deconvoluted into two components. The lower binding energy component (O1s-1) located at about 530.3 eV is attributed to O^{2-} ions on the wurtzite structure surrounded by Zn^{2+} atoms in tetrahedral sites, located mainly in the core region. The second component (O1s-2) is associated with O^{2-} ions in the oxygen deficient regions within the ZnO matrix and/or to the formation of −OH groups chemisorbed (as observed by FTIR) on the surface, indicating the presence of loosely bound oxygen and/or oxygen vacancies/defects near the surface of ZnO nanoparticles.[52,58,59] Thus, according to the XPS and EDX results along with the XRD, FTIR and absorption spectroscopy measurements, the RTFM in pure ZnO could be related to the presence of vacancies/defects located mainly near the surface of ZnO nanoparticles and not to the presence of traces of magnetic impurities.

The RT and 5K M vs H curves of all Fe doped ZnO samples (along with that of $ZnFe_2O_4$) annealed at 550 °C for 1 h are shown in Figure 8. In $Zn_{1-x}Fe_xO$ ($0.0< x <0.10$) nanoparticles the hysteresis loops at RT consist of a linear part due to paramagnetic (PM) contribution, and an open curve due to FM contribution. These data support that all Fe doped ZnO samples are weakly RTFM. With increasing Fe dopant concentration, the PM component increases from 7.14 x 10^{-7} emu/gOe for $x = 0.01$ to 9.64 x 10^{-6} emu/gOe for $x = 0.10$, which indicates higher presence of isolated Fe^{3+} ions, not participating in the magnetic ordering. The RT M vs H curve of $ZnFe_2O_4$ prepared as reference showed superparamagnetic-like (SPM) and PM-like contributions with no coercive at RT. From insets of Figure 8, hysteresis loops at 5K of Fe doped ZnO samples with 1 and 3 at. % showed a linear behavior. For nominal doping concentrations of 5 % and above, a clear hysteresis loops is observed, which increases with increasing iron concentration, displaying a behavior similar to that of $ZnFe_2O_4$ at 5 K. Therefore, the ^{57}Fe Mössbauer measurements together with the magnetization results indicate that some iron ions are present as $ZnFe_2O_4$ from 5 at % onwards and that the solubility limit of Fe ions in ZnO lattice is in fact lower than 5 at % at these conditions. Figure 9 shows the RT M vs H curves of $Zn_{1-x}Fe_xO$ ($0.0< x <0.10$) samples, where the linear component has been subtracted (M-χ_p vs H) to illustrate the actual M_s and coercive field (H_c). Well defined hysteresis loops are observed in all Fe doped ZnO samples, further corroborating the FM behavior. Additionally, the high symmetry of H_c about the zero field (see upper inset of Figure 9) rule out the possibility of existence of exchange bias as reported by Liu *et. al.*[7] The lower inset of Figure 9 corroborates the SPM behavior of $ZnFe_2O_4$. It worth mentioning that M_s of $Zn_{0.99}Fe_{0.01}O$ increased ~4.3 fold in comparison to undoped ZnO sample, indicating that the dopant Fe ions indeed play an important role in the magnetic properties.

The variations of M_s and H_c with the Fe nominal doping are depicted in Figure 10. One can notice that M_s decreases initially as Fe concentration increases from 0.01 to 0.03 and then increases with increasing Fe doping from 0.03 onwards. Ahmed *et al.*[13] have found that increasing the Fe content beyond 5 at. % resulted in a decrease in the magnetization value, which was ascribed to increase of $ZnFe_2O_4$. However, our results showed an opposite trend, because as $ZnFe_2O_4$ appears and increases (see the area values of the D3 component in Table 1) M_s also increases. This result suggests that the increase in M_s and the decrease in H_c, from 5% at. can be due to the formation of disordered $ZnFe_2O_4$ impurity phase. We believe that the very low thermal energy used in this work during annealing treatment (550 ^oC for 1h) helps that Fe^{3+} ions cannot be totally located in the [B] sites and that some Fe^{3+} ions preferentially might occupy the (A) sites in $ZnFe_2O_4$ phase. Then, when a metastable phase with a mixed spinel structure is present, the superexchange interaction (J_{AB}) between the Fe^{3+} ions distributed in tetrahedral and octahedral sites give rise to antiparallel moments, presenting FiM behavior. The reduction of H_c in $Zn_{1-x}Fe_xO$ samples with ≥ 0.05 can be attributed to the influence of the cationic stoichiometry and occupancy in the specific sites of Fe^{3+} in $ZnFe_2O_4$ with increasing Fe content. It is important to point out that in this work a direct relation between Δ D2 and M_s is not observed. It is noted that with increasing Fe concentration from 1% to 3 %, Δ D2 increases, which is attributed to Fe^{3+} replacing Zn^{2+}in high distorted tetrahedral sites, while M_s decreases. In this case the presence of vacancies/defects in ZnO structure might give rise to resultant magnetization in $Zn_{1-x}Fe_xO$ sample with x= 0.01, but when Fe concentration is increased to 3 at. %, superexchange interactions between Fe^{3+} ions might dominate, enhancing the AFM interaction and decreasing the FM behavior.

Figure 11 shows the ZFC and FC curves for Fe doped ZnO samples along with $ZnFe_2O_4$ annealead for 1 h. The curves of $Zn_{1-x}Fe_xO$ samples with 1 and 3 % doping concentration show an almost concave shape. These curves were fitted following the modified Curie-Weiss law, $\chi=\chi_o+C/(T+\theta)$ where χ_o represents non-paramagnetic contributions, $C=Nu^2/3K_B$ (N is the number of magnetic ions/g, u=is the magnetic moment of the ion, K_B is the Boltzmann constant) and θ is the Curie-Weiss temperature. Only positive values for θ were obtained indicating that the isolated-disordered Fe^{3+} ions in $Zn_{1-x}Fe_xO$ are under AF interaction. Moreover, θ increases with Fe doping indicating a progressive increment of the AFM contribution as Fe concentration increases. It is also found that χ_o decreases with x suggesting a decrease in the number of interacting magnetic ions, in full agreement with the M-χ_p vs H results. Now, from 5 % Fe doping onwards, the M vs T curves do not fit the modified Curie-Weiss law, rather tend progressively to deviate, and behave in similar way to that of $ZnFe_2O_4$, but with no presence of the blocking temperature at lower temperatures. The absence of this cusp at about 15 K in the M vs T curves of $Zn_{1-x}Fe_xO$ samples with x= 0.05, 0.08 and 0.10, may indicate that the $ZnFe_2O_4$ formed in these samples is indeed a disordered spinel with a FiM behavior. In our case, the ^{57}Fe Mössbauer and magnetic results provided a strong proof of dopant incorporation into the ZnO structure at least up to 3 at % and that a disordered spinel $ZnFe_2O_4$ impurity phase is observed from 5 at % onwards. Several works have reported an enhancement of magnetization and a reduction of coercive field values with increasing iron doping concentration and that this depends on the nanometric size and magnetic interaction among the particles.[18] Although we have observed this trend from 5% Fe doping onwards, with the tools used in this work, we have observed that such behavior is more probably due to the presence of $ZnFe_2O_4$ with a disordered spinel structure.

Figure 12 shows the RT and 5 K *M* vs *H* curves of Fe doped ZnO samples, annealed at 550 ^{o}C for 3 h. Hysteresis loops at 5K for Fe doped ZnO samples at 1 and 3 at. % showed an almost linear behavior and from 5 at.% onwards an increase in H_c was observed in comparison to those Fe doped samples annealed for 1h (see insets in Figure 8). It is also noticed that the very weak FM behavior, which was observed at RT in the samples with *x* beyond 0.05 and annealed for 1 h, almost vanishes in samples annealed for 3 h and turns into SPM-PM like behavior. Figure 13 shows the RT M-χ_p vs *H* curves of Fe doped ZnO samples annealed for 3 h, where the PM component has been subtracted. Inset of Figure 13 shows the plot of M_s and H_c vs. Fe doping concentration. It is observed that as Fe doping concentration increases M_s decreases. Interestingly, in ZnO samples with Fe dopant % of 1 and 3 % annealed for 3h, the M_s increases by a factor of about ~2.3 in comparison to those samples annealed for 1h. These results suggest that in these nanoparticles, the annealing time is crucial for stabilizing the RTFM. In these 3h annealed $Zn_{1-x}Fe_xO$ ($0.05< x <0.10$) samples, a decrease in M_s and a drastic reduction in the coercive field were observed as *x* increases.

ZFC - FC magnetization curves for the applied field value H = 500 Oe from 5 to 300 K of Fe doped ZnO samples annealed for 3 h are shown in Figure 14. A difference in the ZFC and FC was observed in $Zn_{0.99}Fe_{0.01}O$ sample (see inset of Figure 14), however we did not observe such a difference for $Zn_{0.97}Fe_{0.03}O$ sample. The observed splitting between ZFC and FC curves in $Zn_{0.99}Fe_{0.01}O$ sample could be related to FM behavior, while the no irreversibility between FC and ZFC curves in $Zn_{0.97}Fe_{0.03}O$ sample, could be due to the increases in the AFM coupling between iron ions. *M* vs *T* curves of these samples show that the modified Curie-Weiss law remains comparable to those for the samples annealed for 1h.

Now, in the ZFC curves for $Zn_{1-x}Fe_xO$ samples with $x \geq 0.05$ there is a cusp at about 10 K. This peak can be attributed to two reasons. First, it may be an indication of blocking of SPM particles or may also be due to the existence of spin glass behavior. Due to that these samples did not present appreciable open hysteresis loops in M-χ_p vs H curves at RT and by comparing with $ZnFe_2O_4$ sample, clearly this phenomenon can be attributed to a SPM behavior of $ZnFe_2O_4$. According to our magnetic results in $Zn_{1-x}Fe_xO$ samples with $x \geq 0.05$, the increase in annealing time helps the Fe^{3+} ions to be located in the [B] site of $ZnFe_2O_4$, producing a structural re-arrangement and then leading to more stable $ZnFe_2O_4$ phase. When the thermal energy is not enough, then a metastable $ZnFe_2O_4$ phase with a disordered structure is produced.

4. DISCUSSION

The analysis of the data collected using the various techniques suggested that undoped and the Fe doped ZnO samples with $x \leq 0.03$, annealed for 1 h and 3 h are pure and free of both iron oxides and clustering of Fe dopant. $ZnFe_2O_4$ was the only impurity phase identified in all the Fe doped ZnO samples with $x \geq 0.05$. For samples annealed for 1h this impurity phase was found to be in a disordered state, i.e. Zn^{2+} and Fe^{3+} were distributed amongst both octahedral and tetrahedral sites, and therefore an effective FiM signal was detected. With increasing annealing time, this FiM signal decreased which was reflected in the lower M_s values, therefore suggesting a more ordered $ZnFe_2O_4$ structure. These results suggested that for this method of synthesis the solubility limit of Fe in ZnO lies in the range of 3 to 5 at. %.

We have detected weak RTFM signal in undoped ZnO nanoparticles. The origin of this signal has been debated, both theoretically and experimentally, for a long time, and it is still an unsolved question. Different types of intrinsic defects have been proposed as the main sources of magnetism. For example, Xu *et al.*[55] proposed that the magnetism is due to V_O^+, located mainly near the surface of the ZnO nanoparticles. Here it is interesting to mention that the theoretical works by Lany *et al.* predicted that V_O in thermal equilibrium is deep and does not provide *n*-type doping, whereas under certain conditions, metastable shallow state of V_O can exist, which could contribute to *n*-type conductivity.[60,61] On the other hand, Wang *et al.*[62] have shown that V_{Zn}, instead of V_O are the main source of the RTFM signal. Moreover they indicated that the magnetic moment is originated from unpaired 2p electrons at the oxygen sites located in the immediate vicinity of V_{Zn}. Very recently, Motaung *et al.*[54] proposed that both V_{Zn} and V_O^+, located mainly on the ZnO nanoparticle surface play a vital role in the observed ferromagnetism in this system. On the contrary, for Zhang *et al.*[63] Zn interstitial, Zn_i, plays an important role in triggering magnetic order. Another different mechanism has been proposed by Sanchez *et al.*[64] and Gallego *et al.*[65] who predicted that the magnetic moments mainly reside in the oxygen-ended polar terminations at the surface of ZnO nanoparticles and their origin is related to the existence of spin polarized *p* holes at the valence band. For these authors, absorbed hydrogen can lead to extinction of the magnetism[66]. Finally, for Schoenhalz *et al.*[67] the FM in ZnO nanostructures should be mediated by extended defects such as surfaces and grain boundaries, and not by point defects. In the case of our work, single charged V_O^+, V_{Zn} and O-ended polar terminations are the most probable sources of the RTFM in ZnO.

We have found that the Fe ions in Fe doped ZnO samples exist only in the 3+ oxidation state, and they are in high spin state, and also they have substitutional occupancy at the Zn^{2+} sites in the core, in tetrahedral coordination, and in the surface of the nanoparticles, presumably in pseudo-octahedral coordination. Our results pointed out that in these nanoparticles there exist isolated Fe^{3+} ions that do not interact ferromagnetically at RT. The absence of Fe^{2+} in this work could be explained from the preparation method and starting reactants used. The process involves the aqueous reaction of Zn^{2+} and Fe^{3+} ions with CA to produce high stability complexes, where the initial oxidation states of the cations are retained. When heated with EG, these chelates undergo esterification reaction and form a polymeric resin in which the cations are embedded. Additional heating of the resin in air allows the slow removal of the organic components in an oxidative environment, which avoids the reduction/conversion of Fe^{3+} to Fe^{2+}. We also found that with increasing Fe content, M_s decreases and for $x \geq 0.05$ the samples become contaminated with disordered $ZnFe_2O_4$. In fact, if the solubility limit of Fe^{3+} in pseudo-octahedral site is overpassed a weak impurity phase of $ZnFe_2O_4$ appears. Another very interesting observation was that M_s for $Zn_{1-x}Fe_xO$ with $x \leq 0.03$ increased with increasing annealing time from 1 to 3h (maintaining the same annealing temperature of 550 ^{o}C), suggesting specific defect concentration ranges for FM signal, where annealing time could stabilize defect/vacancies in these Fe doped ZnO samples.

Now, the apparent discrepancy between the results of the magnetization measurements and Mössbauer spectrometry, for which the first technique detect a FM signal while the second one did not show a sextet in any spectrum, needs further discussion. Mishra and Das[22] have proposed that this discrepancy can be explained as due to the huge difference between the measurement time scales of the two techniques (∼100 s for magnetization and $\sim 10^{-8}$ s for Mössbauer spectroscopy). However, this explanation requires the presence of dynamics effects, like superparamagtism or other similar dynamic phenomena, which was not evidenced at RT in our impurity-free samples. Another explanation to the discrepancy is also possible for which the effective magnetic field at the site of the ^{57}Fe nucleus is so weak or do not exist at all. The effective magnetic field can have different origins, such as: external applied magnetic field, demagnetizing field, Lorentz field, dipolar interaction of the nucleus with the spin moment of the atom, the Fermi contact, and interaction of the nucleus with the orbital magnetic moment of the parent atom. It is well documented in the literature that, except the Fermi contact and in some cases the orbital atomic moment, the contributions of most mentioned fields to the total effective magnetic field are weak. [68] The Fermi contact arises due to the interaction of the ^{57}Fe nucleus with intrinsic impairing of the actual *s*-electrons, or indirectly as a result of polarisation effects on filled *s*-orbitals. This can occur if the neighbor atom has unpaired electrons in *d* orbitals or if it is chemically bonded to such an atom. In some cases, the direct conduction-electron polarisation as well as indirect core-polarisation effects may also contribute[68]. Therefore, the FM signal observed in the samples by the magnetization measurements cannot be originated from the Fe ions but should have another origin.

The origin of the RTFM signal in Fe doped ZnO nanoparticles, similar to the undoped ZnO case, is still an unsolved question. Several models have been put forward to explain it. Let us briefly discuss some of them. Coey *et al.*[69] proposed that long range FM ordering in oxide DMS can be due to the overlapping of bound magnetic polarons. These polarons are formed by magnetically interacting neighboring magnetic ions, in our case Fe, whose interactions are mediated by an F center. In turn, this F center can be created by an electron trapped in a defect, such as a V_O. This model has been used by Inamdar *et al.*[27] and Ahmed *et al.*[13] to explain the observed ferromagnetism in Fe doped ZnO nanocrystals. This bound magnetic polaron model does not seem to explain the increase in the RTFM signal with increasing annealing time as observed in our samples. In fact, we could expect that with increasing annealing time, the number of V_O decreases, therefore reducing the FM interaction. Another model has been proposed by Karmakar *et al.*[16] They argued that Fe in ZnO is present in both valence states, Fe^{2+} and Fe^{3+}, and that the presence of the latter requires the existence of V_{Zn}. Their theoretical calculations suggested that hole doping, induced by V_{Zn}, is crucial to promote FM in this system. In fact this defect mediates the exchange interactions between the Fe ions. It is worth mentioning that we could not detect the presence of Fe^{2+}, therefore we cannot use this model to explain the observed RTFM in our samples. The above mentioned models require the participation of Fe in the RTFM signal. However, as mentioned before, our results pointed out that Fe does not participate in the FM signal. Therefore we need to search for other type of models. One of them is the charge transfer ferromagnetic model, recently proposed by Coey *et al.*[70,71] This model requires the existence of a defect-based band having a peak in the density of states (DOS) close to the Fermi level, a charge reservoir for transferring electrons, and an effective exchange integral associated with the defect states. The first component, *i.e.* the defect based band in our samples, can originate from some regions in the nanoparticles in which the extended defects are concentrated. It is likely that in our samples this FM regime is limited to the defects rich surface region of the nanoparticles, while the core of the particle remains in other magnetic states. In relation to the second component, the local charge reservoir can be some kind of defects acting as reservoirs to transfer electrons, bringing the Fermi level up to a maximum in the density of states provoking exchange Stoner splitting of the DOS.

There is also another possible model which was already presented when we discussed the origin of the RTFM signal in undoped ZnO nanoparticles. This model was based upon the existence of several kinds of defects that can become magnetic. In this case, the effect of Fe in the magnetism of Fe doped ZnO samples is to increase the presence of such kind of defects, in comparison to the undoped samples. Theoretical studies by Debernardi and Fanciulli[72] and experimental studies by Azamat and Fanciulli[73] reported that V_{Zn} and V_O are required to charge compensate for the Fe^{3+} substitution. They found that Fe_{Zn}–V_{Zn}, where V_{Zn} occupies the next nearest neighbor position to Fe atom, is energetically favored in comparison to isolated Fe_{Zn} and V_{Zn}. An opposite situation was obtained for Fe_{Zn} and V_O. The authors proposed that Fe_{Zn}–V_{Zn} provides a key to understand the magnetism of Fe doped ZnO. Now, on the other hand, we have found that with increasing Fe content, the average grain size decreases and therefore the surface area increases, and in turn more oxygen ended terminations are expected. As mentioned above, Sanchez *et al.*[64] and Gallego *et al.*[65] proposed that the magnetic moments mainly reside in these O-ended polar terminations and their origin is related to the existence of spin polarized p holes at the valence band. Now, one could expect that with increasing iron doping more of these defects should be present, and therefore greater M_s should be expected, however this was not observed. This behavior can partly be understood if AF coupling between the disordered Fe^{3+} spins present in $Zn_{1-x}Fe_xO$ increase with increasing Fe concentrations.

5. CONCLUSIONS

In summary, we investigated in detail the crystallographic, optical and magnetic properties of Sol-Gel synthesized undoped and Fe doped ZnO nanopowders. RTFM was observed in pure ZnO and it has been attributed to concomitant contributions coming from metastable V_O^+, V_{Zn}, and O-ended polar terminations near at the nanoparticle's surface. In comparison to the undoped ZnO sample, by doping with 1 at. % of Fe, the M_s value increased about 2.3 times. High spin Fe^{3+} substituted Zn^{2+} in the core as well as at the surface of the ZnO nanoparticles, and its presence increased the surface area, decreased the band gap, and also decreased the unit cell parameters. We report experimental evidence of FM signal enhancement in Fe doped ZnO nanopartciles, for which Fe do not contribute directly into this FM signal, but it contributed to the additional formation of several defects such as V_O, V_{Zn}, O-ended polar terminations, and OH^- groups. Therefore we associated the observed magnetism to the concentration of defects preferentially in the surface of the nanoparticles. The interesting observation that the increment of thermal annealing time from 1h to 3h increased the FM signal was probably due to that fact that more Fe ions were diffused towards the surface of the nanoparticles and therefore provoked greater concentration of the defects in this region. Additional Fe doping ($x \geq 0.03$) did not increase the FM signal, but on the contrary decreased it, which was assumed to be due to the formation of AFM interactions between neighboring Fe ions, which suppressed the RTFM. For $x \geq 0.05$, disordered $ZnFe_2O_4$ spurious phase was formed, placing the solubility limit of Fe for these samples in the $0.03 \leq x \leq 0.05$ range.

ACKNOWLEDGMENTS

This study was supported in Colombia by CODI-University of Antioquia (Sustainability Program for the Solid State Group 2014-2015 and project IN645CE). One of the authors (J.J.Beltrán) thanks Gobernación del Cesar by technical cooperation agreement No 0.38 2006 Colciencias-Universidad Popular del Cesar in association with the Universidad de Antioquia. Research at Boise State University was supported by NSF CBET 1134468, NSF EAGER DMR-1137419, and ARO W911NF-09-1-0051 grants.

AUTHOR INFORMATION

Corresponding Author

* *jjbj08@gmail.com*

Author Contributions

All authors have given approval to the final version of the manuscript.

NOTES

The authors declare no competing financial interest.

REFERENCES

1 T. Dietl, H. Ohno, F. Matsukura, J. Cibert and D. Ferrand, *Science*, 2000, **287**, 1019–1022.

2 J. Kaur, R. K. Kotnala, V. Gupta and K. Chand, *Curr. Appl. Phys.*, 2014, **14**, 749–756.

3 X. Chen, Z. Zhou, K. Wang, X. Fan, S. Hu, Y. Wang and Y. Huang, *Mater. Res. Bull.*, 2009, **44**, 799–802.

4 Y. Q. Wang, S. L. Yuan, L. Liu, P. Li, X. X. Lan, Z. M. Tian, J. H. He and S. Y. Yin, *J. Magn. Magn. Mater.*, 2008, **320**, 1423–1426.

5 A. Franco and T. E. P. Alves, *Mater. Sci. Semicond. Process.*, 2013, **16**, 1804–1807.

6 P. Dhiman, J. Chand, A. Kumar, R. K. Kotnala, K. M. Batoo and M. Singh, *J. Alloys Compd.*, 2013, **578**, 235–241.

7 H. Liu, J. Yang, Y. Zhang, Y. Wang and M. Wei, *Mater. Chem. Phys.*, 2008, **112**, 1021–1023.

8 Y. Lin, D. Jiang, F. Lin, W. Shi and X. Ma, *J. Alloys Compd.*, 2007, **436**, 30–33.

9 M. J. Akhtar, M. Nadeem, S. Javaid and M. Atif, *J. Phys. Condens. Matter*, 2009, **21**, 405303.

10 V. Blanco-Gutiérrez, F. Jiménez-Villacorta, P. Bonville, M. J. Torralvo-Fernández and R. Sáez-Puche, *J. Phys. Chem. C*, 2011, **115**, 1627–1634.

11 J. H. Shim, T. Hwang, S. Lee, J. H. Park, S.-J. Han and Y. H. Jeong, *Appl. Phys. Lett.*, 2005, **86**, 082503.

12 S. K. Mandal, A. K. Das, T. K. Nath and D. Karmakar, *Appl. Phys. Lett.*, 2006, **89**, 144105.

13 F. Ahmed, S. Kumar, N. Arshi, M. S. Anwar and B. Heun Koo, *CrystEngComm*, 2012.

14 A. Debernardi and M. Fanciulli, *Appl. Phys. Lett.*, 2007, **90**, 1–4.

15 N. Ganguli, I. Dasgupta and B. Sanyal, *Appl. Phys. Lett.*, 2009, **94**, 192503.

16 D. Karmakar, S. Mandal, R. Kadam, P. Paulose,A. Rajarajan, T. Nath, A. Das, I. Dasgupta and G. Das, *Phys. Rev. B*, 2007, **75**, 144404.

17 H. Liu, J. Yang, Y. Zhang, L. Yang, M. Wei and X. Ding, *J. Phys. Condens. Matter*, 2009, **21**, 145803.

18 R. Saleh, S. P. Prakoso and A. Fishli, *J. Magn. Magn. Mater.*, 2012, **324**, 665–670.

19 M. D. Carvalho, L. P. Ferreira, R. P. Borges and M. Godinho, *J. Solid State Chem.*, 2012, **185**, 160–165.

20 S. Kumar, Y. J. Kim, B. H. Koo, S. K. Sharma, J. M. Vargas, M. Knobel, S. Gautam, K. H. Chae, D. K. Kim, Y. K. Kim and C. G. Lee, *J. Appl. Phys.*, 2009, **105**, 07C520.

21 M. V. Limaye, S. B. Singh, R. Das, P. Poddar and S. K. Kulkarni, *J. Solid State Chem.*, 2011, **184**, 391–400.

22 A. K. Mishra and D. Das, *Mater. Sci. Eng. B*, 2010, **171**, 5–10.

23 J. F. Piamba, J. C. Paz, L. E. Zamora and G.A. Pérez Alcázar, *J. Supercond. Nov. Magn.*, 2012, **25**, 2223–2226.

24 F. Lin, D. Jiang and X. Ma, *Phys. B Condens. Matter*, 2010, **405**, 1466–1469.

25 A. Samariya, R. K. Singhal, S. Kumar, Y. T. Xing, M. Alzamora, S. N. Dolia, U. P. Deshpande, T. Shripathi and E. B. Saitovitch, *Mater. Chem. Phys.*, 2010, **123**, 678–684.

26 D. Wang, Z. Q. Chen, D. D. Wang, J. Gong, C. Y. Cao, Z. Tang and L. R. Huang, *J. Magn. Magn. Mater.*, 2010, **322**, 3642–3647.

27 D. Y. Inamdar, A. K. Pathak, I. Dubenko, N. Ali and S. Mahamuni, *J. Phys. Chem. C*, 2011, **115**, 23671–23676.

28 P. K. Sharma, R. K. Dutta, A. C. Pandey, S. Layek and H. C. Verma, *J. Magn. Magn. Mater.*, 2009, **321**, 2587–2591.

29 J. J. Beltrán, J. A. Osorio, C. A. Barrero, C. B. Hanna and a. Punnoose, *J. Appl. Phys.*, 2013, **113**, 17C308.

30 J. J. Beltrán, C. A. Barrero and A. Punnoose, *J. Phys. Chem. C*, 2014, **118**, 13203–13217.

31. Pechini MP (1967) US Patent 3,330,697, 11 July 1967.

32 H. Morkoç and Ümit Özgü., WILEY-VCH Verlag GmbH & Co. KGaA, Weinheim, 2009.

33 M. Gaudon, O. Toulemonde and A. Demourgues, *Inorg. Chem.*, 2007, **46**, 10996–1002.

34 Shannon, R. D.; Prewitt, C. T. *Acta Crystallogr.*, 1969, B25, 925−946. Shannon, R. D. *Acta Crystallogr.*, 1976, A32,751−767.

35 S. Kumar, S. Mukherjee, R. Kr. Singh, S. Chatterjee and A. K. Ghosh, *J. Appl. Phys.*, 2011, **110**, 103508.

36 A. Punnoose, K. Dodge, J. W. Rasmussen, J. Chess, D. Wingett and C. Anders, *ACS Sustain. Chem. Eng.*, 2014, **2**, 1666–1673.

37 D. Stoltz, P. Palmgren, S. Yu, M. Go and U. O. Karlsson, *J. Phys. Chem. C*, 2010, 11157–11161.

38 K. J. Kim and Y. R. Park, *J. Appl. Phys.*, 2004, **96**, 4150.

39 D. Y. Inamdar, A. D. Lad, A. K. Pathak, I. Dubenko, N. Ali and S. Mahamuni, *J. Phys. Chem. C*, 2010, **114**, 1451–1459.

40 A. Escobedo, E. Sánchez and U. Pal, *Rev. Mex. Física*, 2007, **53**, 18–22.

41 S. Dutta, S. Chattopadhyay, M. Sutradhar, A. Sarkar, M. Chakrabarti, D. Sanyal and D. Jana, *J. Phys. Condens. Matter*, 2007, **19**, 236218.

42 C. Aydın, M. S. Abd El-sadek, K. Zheng, I. S. Yahia and F. Yakuphanoglu, *Opt. Laser Technol.*, 2013, **48**, 447–452.

43 M. M. Ba-Abbad, A. A. H. Kadhum, A. B. Mohamad, M. S. Takriff and K. Sopian, *Chemosphere*, 2013, **91**, 1604–11.

44 J. Anghel, A. Thurber, D. A. Tenne, C. B. Hanna and A. Punnoose, *J. Appl. Phys.*, 2010, **107**, 09E314.

45 Y. Sun, J. B. Ketterson and G. K. L. Wong, *Appl. Phys. Lett.*, 2000, **77**, 2322.

46 F. Li, H. Wang, L. Wang and J. Wang, *J. Magn. Magn. Mater.*, 2007, **309**, 295–299.

47 D. Pooja, S. Sharma, M. Knobel, R. Rani and M. Singh, *Res. J. Recent Sci.*, 2012, **1**, 48–52.

48 E. Murad, and J. Cashion, "*Mössbauer spectroscopy of environmental materials and their industrial utilization*", Kluwer Academic Publishers, Boston, 2004.

49 J. Zhang, S. Xiong, X. Wu, A. Thurber, M. Jones, M. Gu, Z. Pan, D.A. Tenne, C. B. Hanna, Y. Du and A. Punnoose, *Phys. Rev. B*, 2013, **88**, 085437.

50 M. A Garcia, J. M. Merino, E. Fernández Pinel, a Quesada, J. de la Venta, M. L. Ruíz González, G. R. Castro, P. Crespo, J. Llopis, J. M. González-Calbet and A. Hernando, *Nano Lett.*, 2007, **7**, 1489–94.

51 S. Kumar, Y. Kim, B. Koo, S. Gautam, K. Chae, R. Kumar and C. Lee, *Mater. Lett.*, 2009, **63**, 194–196.

52 X. Bie, C. Wang, H. Ehrenberg, Y. Wei, G. Chen, X. Meng, G. Zou and F. Du, *Solid State Sci.*, 2010, **12**, 1364–1367.

53 A. Kushwaha, H. Tyagi and M. Aslam, *AIP Adv.*, 2013, **3**, 042110.

54 D. E. Motaung, G. H. Mhlongo, S. S. Nkosi, G. F. Malgas, B. W. Mwakikunga, E. Coetsee, H. C. Swart, H. M. I. Abdallah, T. Moyo and S. S. Ray, *ACS Appl. Mater. Interfaces*, 2014, **6**, 8981–95.

55 X. Xu, C. Xu, J. Dai, J. Hu, F. Li and S. Zhang, *J. Phys. Chem. C*, 2012, **116**, 8813–8818.

56 S. K. S. Parashar, B. S. Murty, S. Repp, S. Weber, E. Erdem, S. K. S. Parashar, B. S. Murty, S. Repp, S. Weber and E. Erdem, 2013, **113712**.

57 P. Jakes and E. Erdem, *Phys. status solidi - Rapid Res. Lett.*, 2011, **5**, 56–58.

58 S. Bian, I. A. Mudunkotuwa, T. Rupasinghe and V. H. Grassian, *Langmuir*, 2011, **27**, 6059–6068.

59 T. Szörényi, L. D. Laude, I. Bertóti, Z. Kántor and Z. Geretovszky, *J. Appl. Phys.*, 1995, **78**, 6211.

60 S. Lany and A. Zunger, *Phys. Rev. B*, 2005, **72**, 035215.

61 S. Lany, J. Osorio-Guillén and A. Zunger, *Phys. Rev. B*, 2007, **75**, 241203.

62 Q. Wang, Q. Sun, G. Chen, Y. Kawazoe and P. Jena, *Phys. Rev. B*, 2008, **77**, 205411.

63 X. Zhang, W. Zhang, X. Zhang, X. Xu, F. Meng and C. C. Tang, *Adv. Condens. Matter Phys.*, 2014, **806327**.

64 N. Sanchez, S. Gallego and M. Muñoz, *Phys. Rev. Lett.*, 2008, **101**, 067206.

65 S. Gallego, J. I. Beltrán, J. Cerdá and M. C. Muñoz, *J. Phys. Condens. Matter*, 2005, **17**, L451–L457.

66 N. Sanchez, S. Gallego, J. Cerdá and M. C. Muñoz, *Phys. Rev. B*, 2010, **81**, 115301.

67 A. L. Schoenhalz, J. T. Arantes, A. Fazzio and G. M. Dalpian, *Appl. Phys. Lett.*, 2009, **94**, 162503.

68 N. N. Greenwood and T. C. Gibb, *Mössbauer spectroscopy.*, Chapman and Hall Ltd., London, 1971.

69 J. M. D. Coey, M. Venkatesan and C. B. Fitzgerald, *Nat. Mater.*, 2005, **4**, 173–9.

70 J. M. D. Coey, K. Wongsaprom, J. Alaria and M. Venkatesan, *J. Phys. D. Appl. Phys.*, 2008, **41**, 134012.

71 J. M. D. Coey, P. Stamenov, R. D. Gunning, M. Venkatesan and K. Paul, *New J. Phys.*, 2010, **12**, 053025.

72 A. Debernardi and M. Fanciulli, *Appl. Phys. Lett.*, 2007, **90**, 212510.

73 D. V. Azamat and M. Fanciulli, *Phys. B Condens. Matter*, 2007, **401-402**, 382–385.

TABLES

Table 1. RT ^{57}Fe Mössbauer parameters of Fe-doped ZnO samples annealed for 1 h, along with those of $ZnFe_2O_4$. Estimated errors are of about ±0.01 mm/s for the isomer shift, δ, the quadrupole splitting, Δ, and the linewidth, Γ, and of about ±2% for the relative area, A. D1, D2, and D3 are doublet 1, doublet 2, and doublet 3, respectively.

Fe doped ZnO	Component	δ (mm/s)	Δ (mm/s)	Γ (mm/s)	A (%)
1% Fe	D1	0,25	0,74	0,54	83
	D2	0,3	1,18	0,36	17
3% Fe	D1	0,3	0,73	0,58	79
	D2	0,27	1,21	0,44	21
5%Fe	D1	0,27	0,91	0,38	70
	D2	0,28	1,53	0,48	17
	D3	0,34	0,37	0,28	13
8%Fe	D1	0,29	0,88	0,42	58
	D2	0,29	1,38	0,36	19
	D3	0,32	0,40	0,32	23
10%Fe	D1	0,29	0,84	0,4	54
	D2	0,29	1,31	0,4	17
	D3	0,32	0,40	0,38	29
$ZnFe_2O_4$	D1	0.34	0.39	0.42	100

FIGURE CAPTIONS

Figure 1. Rietveld refinement analysis of XRD patterns of Fe doped ZnO samples annealed at 550 ºC for 1 h. Solid spheres are experimental data, whereas red solid lines represent the fit. The blue lines below represent the difference pattern. The top panel at the right side shows some selected expanded regions in the 28º to 40º 2θ range plotted in log scale. The arrows point to $ZnFe_2O_4$ peaks.

Figure 2. Variation of **(a)** *a* and *c* lattice parameters **(b)** Zn–O bond length (*L*) parallel to the *c*-axis and **(c)** lattice distortion degree (*R)* and *c/a* ratio as a function of the Fe content for all Fe doped ZnO samples annealed for 1 h.

Figure 3. FTIR spectra of $Zn_{1-x}Fe_xO$ ($0 \leq x \leq 0.05$) samples annealed at 550 °C for 1 h.

Figure 4. a) Optical absorbance spectra of ZnO and Fe doped ZnO samples annealed at 550 °C for 1 h. The inset shows the variation of the calculated band gap and the average crystallite size (*Dv*) with the nominal Fe content. **b)** Derivative of absorbance spectra with respect to wavelength for $Zn_{1-x}Fe_xO$ samples annealed at 550 °C for 1 h.

Figure 5. RT ^{57}Fe Mössbauer spectra of $Zn_{1-x}Fe_xO$ samples annealed at 550 °C for 1 h and of $ZnFe_2O_4$ prepared as reference.

Figure 6. Variations of quadrupole splitting of the D2 (Δ D2) and lattice volume (*V*) as a function of nominal Fe concentration for samples annealed at 550 °C for 1 h.

Figure 7. a) RT hysteresis loops for undoped ZnO after subtracting the diamagnetic background contribution. The inset shows ZFC and FC curves for pure ZnO with H= 500 Oe**. b)** RT EPR spectra of undoped ZnO nanoparticles. The inset shows expanded region of the spectra in the range of 3250 to 3450 G. **c)** Wide survey X- ray photoelectron spectrum of undoped ZnO nanocrystalline. The inset shows high resolution scans of the Mn, Fe, Co and Ni 3p and **d)** Deconvoluted XPS spectra of the core−electron region of O 1s for pure ZnO nanoparticles.

Figure 8. RT hysteresis loops for Fe doped ZnO nanoparticles along with $ZnFe_2O_4$ sample annealed for 1 h. The insets show hysteresis loops at 5 K.

Figure 9. RT Magnetic hysteresis loops (M-χ_p vs H) of $Zn_{1-x}Fe_xO$ samples annealed at 550 ^oC for 1 h. Upper inset shows the low field region of all Fe doped ZnO samples, while lower inset shows M-χ_p vs H curves of $ZnFe_2O_4$.

Figure 10. Variations of coercive field (*Hc*) and saturation magnetization (*Ms*) as a function of nominal Fe concentration for samples annealed at 550 ^oC for 1h. The dashed line represents the *Ms* value of undoped ZnO.

Figure 11. *M(T*) curves with H= 500 Oe for 1, 3, 5, 8 and 10 % Fe doped ZnO samples annealead for 1 h. The symbols (solid lines) correspond to ZFC (FC) data. The inset shows ZFC (FC) curves for $ZnFe_2O_4$.

Figure 12. RT hysteresis loops for Fe doped ZnO nanoparticles along with $ZnFe_2O_4$ sample annealed for 3 h. The insets show hysteresis loops at 5 K.

Figure 13. RT Magnetic hysteresis loops (M-χ_p vs H) of $Zn_{1-x}Fe_xO$ samples annealed for 3 h. The inset shows the variation of *Ms* and *Hc* with the nominal Fe content.

Figure 14. *M(T*) curves with H= 500 Oe for 1, 3 5, 8 and 10 % Fe doped ZnO samples annealead for 3 h. The symbols (solid lines) correspond to ZFC (FC) data. The inset shows ZFC (FC) for 1% Fe doped ZnO sample.

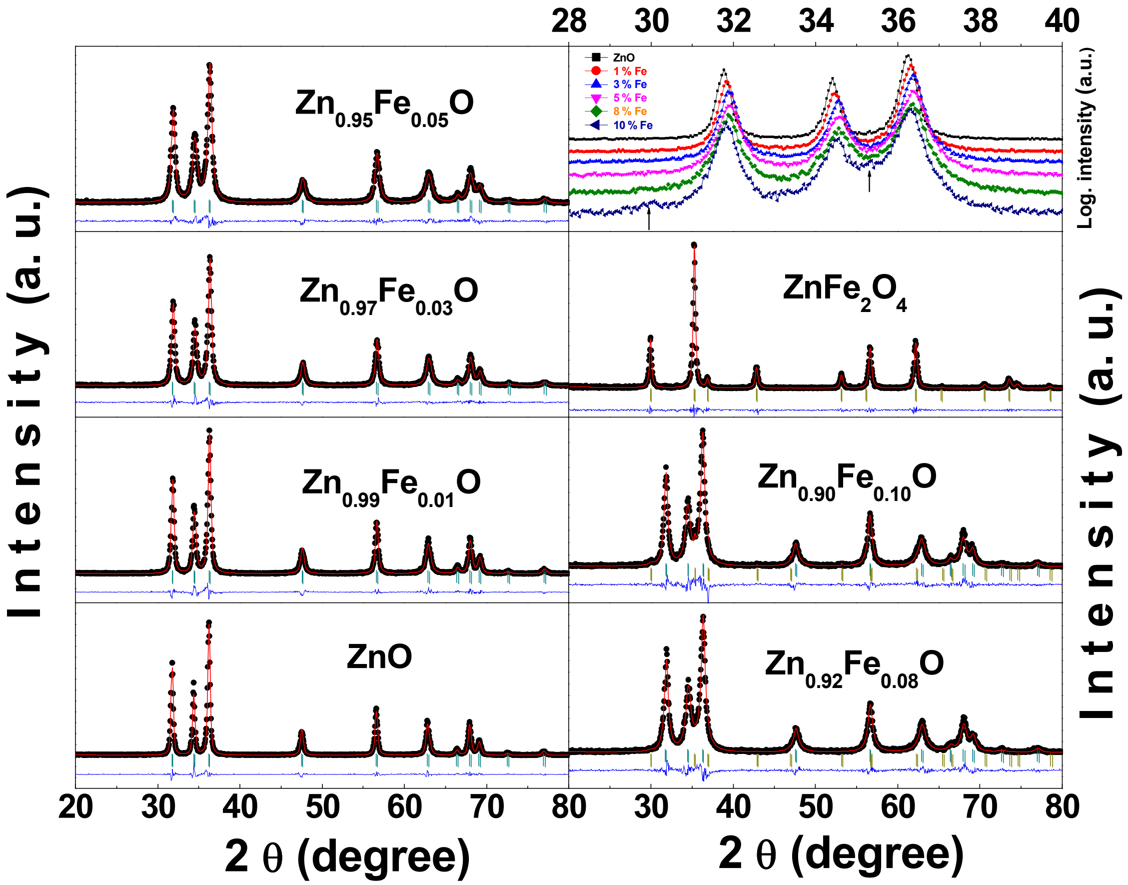

Figure 1. Rietveld refinement analysis of XRD patterns of Fe doped ZnO samples annealed at 550 ºC for 1 h. Solid spheres are experimental data, whereas red solid lines represent the fit. The blue lines below represent the difference pattern. The top panel at the right side shows some selected expanded regions in the 28º to 40º 2θ range plotted in log scale. The arrows point to $ZnFe_2O_4$ peaks.

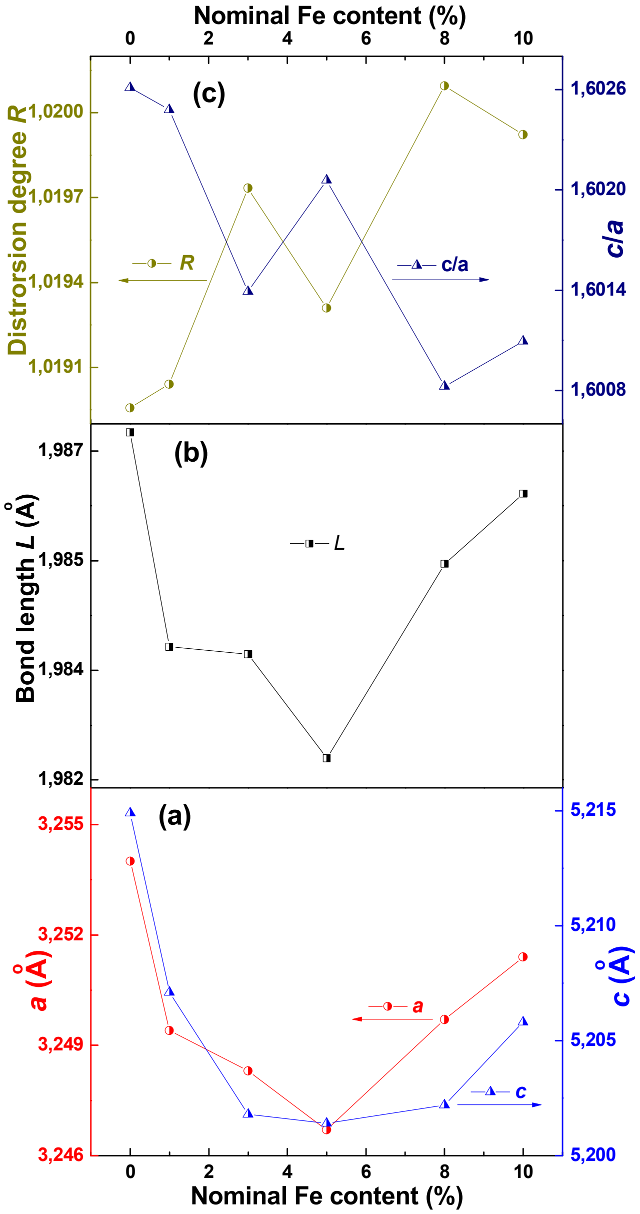

Figure 2. Variation of **(a)** *a* and *c* lattice parameters **(b)** Zn–O bond length (*L*) parallel to the *c*-axis and **(c)** lattice distortion degree (*R)* and *c/a* ratio as a function of the Fe content for all Fe doped ZnO samples annealed for 1 h.

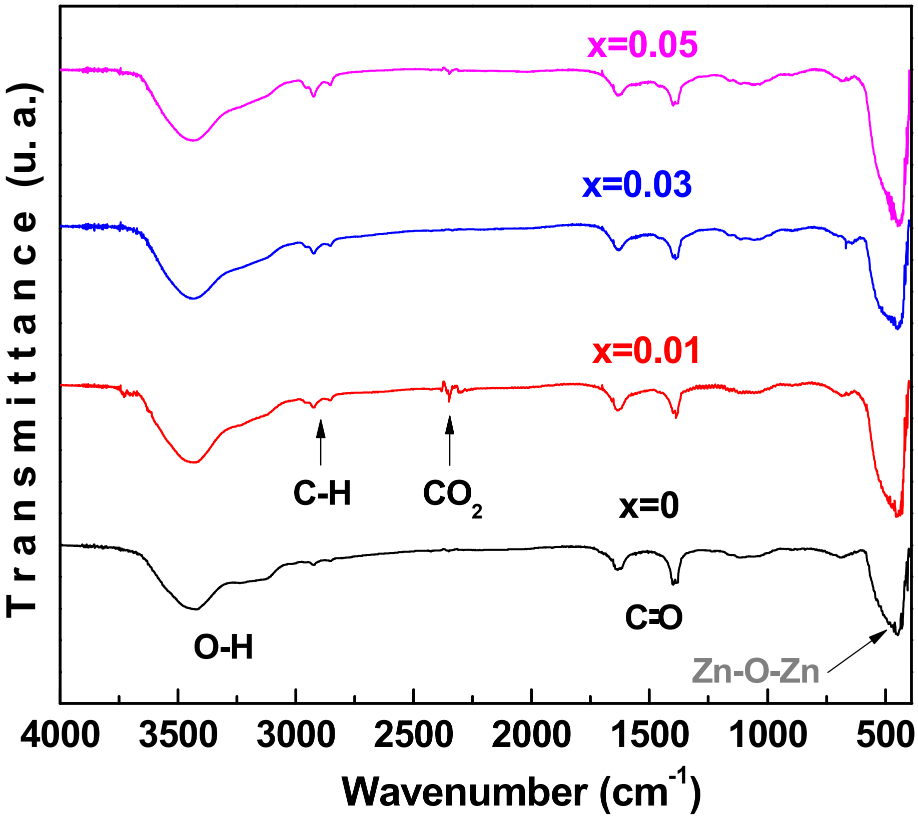

Figure 3. FTIR spectra of $Zn_{1-x}Fe_xO$ ($0 \leq x \leq 0.05$) samples annealed at 550 °C for 1 h.

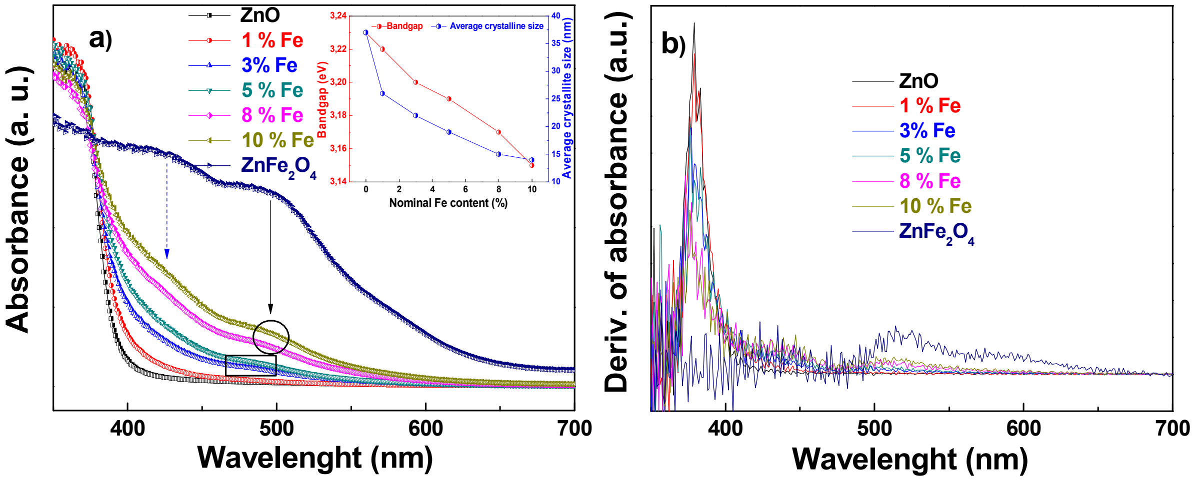

Figure 4. a) Optical absorbance spectra of ZnO and Fe doped ZnO samples annealed at 550 °C for 1 h. The inset shows the variation of the calculated band gap and the average crystallite size (*Dv*) with the nominal Fe content. **b)** Derivative of absorbance spectra with respect to wavelength for $Zn_{1-x}Fe_xO$ samples annealed at 550 °C for 1 h.

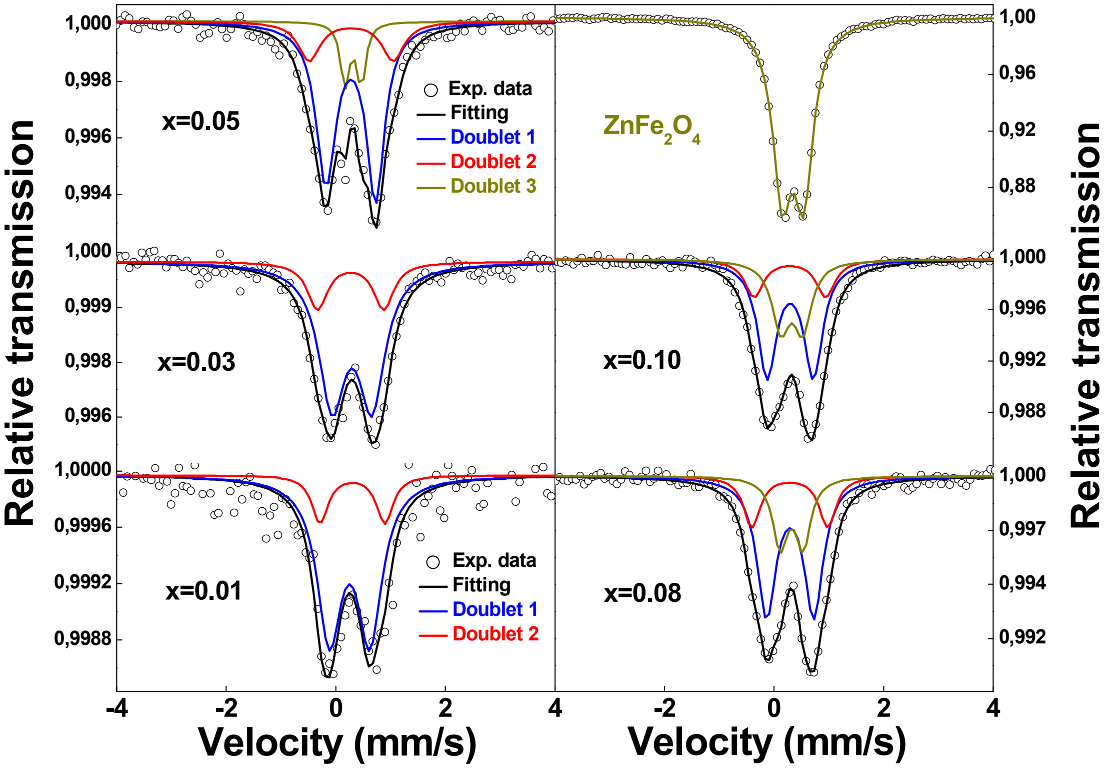

Figure 5. RT ^{57}Fe Mössbauer spectra of $Zn_{1-x}Fe_xO$ samples annealed at 550 ^{o}C for 1 h and of $ZnFe_2O_4$ prepared as reference.

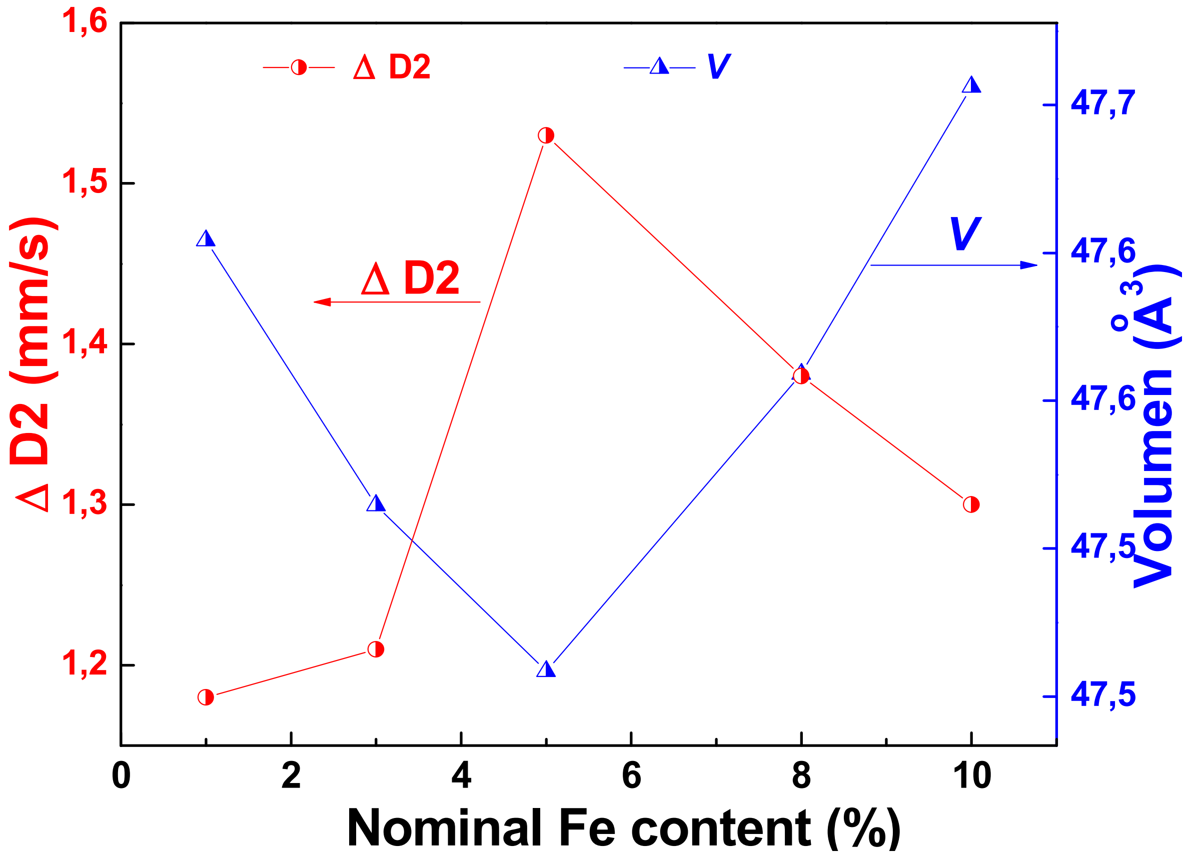

Figure 6. Variations of quadrupole splitting of the D2 (Δ D2) and lattice volume (*V*) as a function of nominal Fe concentration for samples annealed at 550 °C for 1 h.

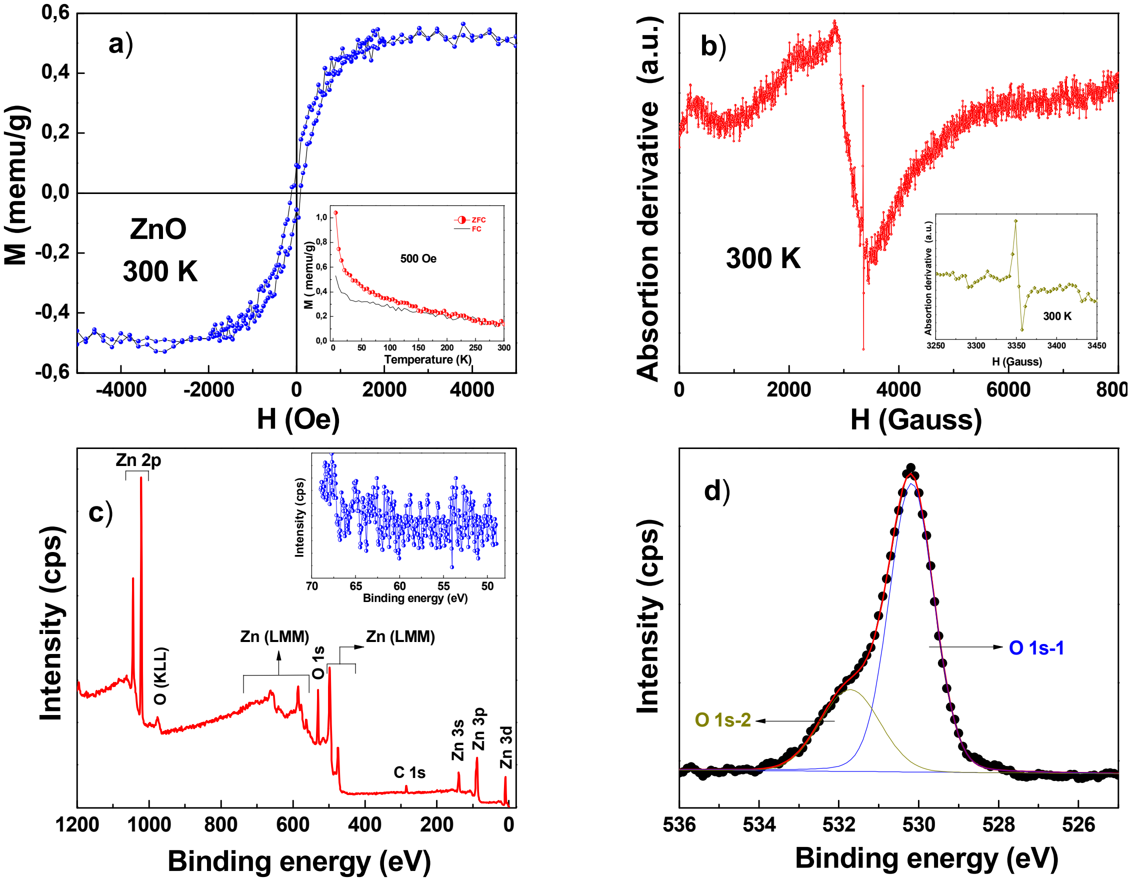

Figure 7. **a)** RT hysteresis loops for undoped ZnO after subtracting the diamagnetic background contribution. The inset shows ZFC and FC curves for pure ZnO with H= 500 Oe**. b)** RT EPR spectra of undoped ZnO nanoparticles. The inset shows expanded region of the spectra in the range of 3250 to 3450 G. **c)** Wide survey X- ray photoelectron spectrum of undoped ZnO nanocrystalline. The inset shows high resolution scans of the Mn, Fe, Co and Ni 3p and **d)** Deconvoluted XPS spectra of the core−electron region of O 1s for pure ZnO nanoparticles.

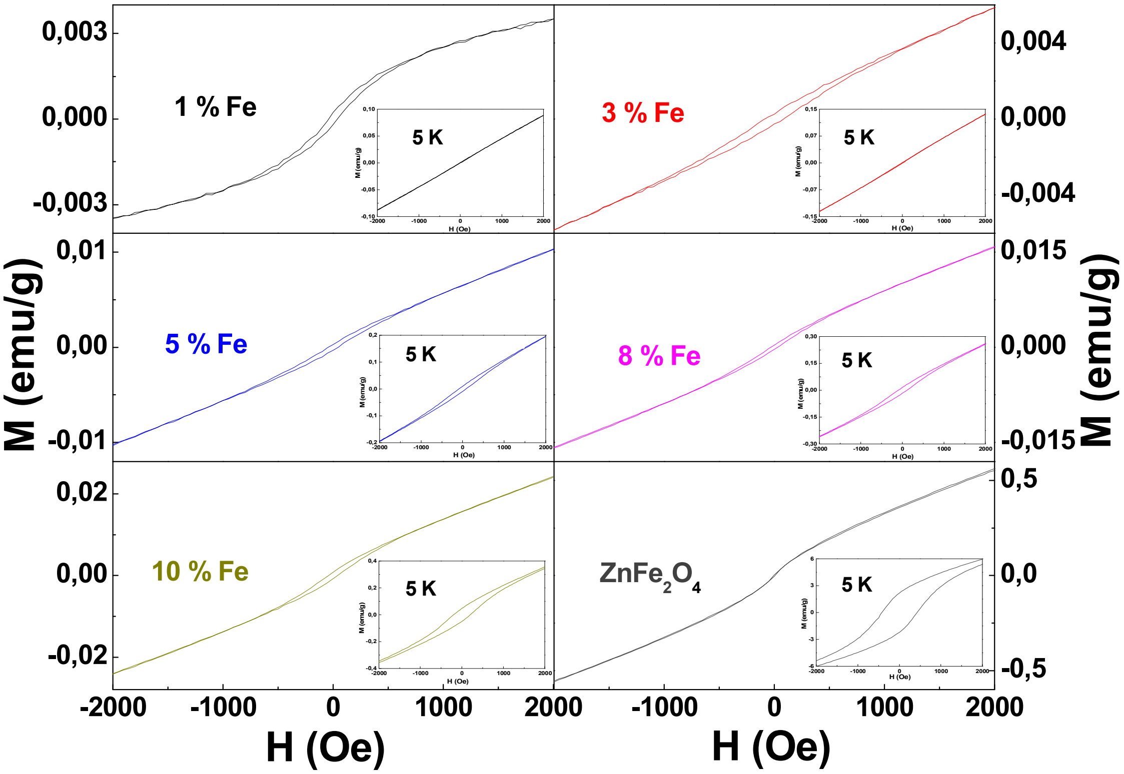

Figure 8. RT hysteresis loops for Fe doped ZnO nanoparticles along with $ZnFe_2O_4$ sample annealed for 1 h. The insets show hysteresis loops at 5 K.

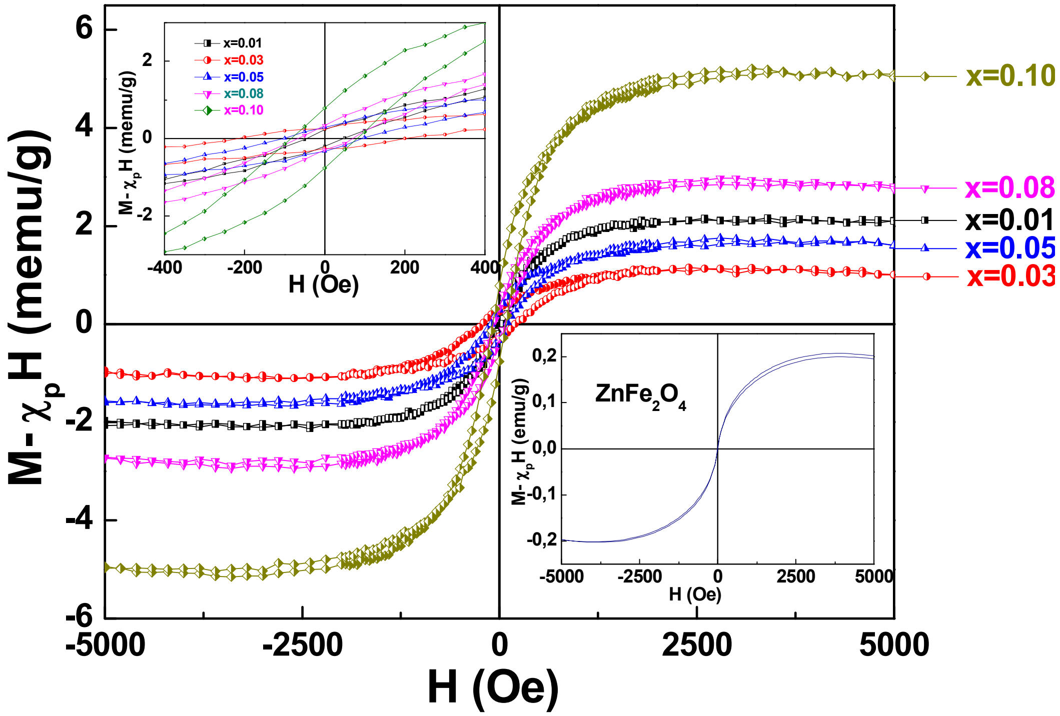

Figure 9. RT Magnetic hysteresis loops (M-χ_p vs H) of $Zn_{1-x}Fe_xO$ samples annealed at 550 °C for 1 h. Upper inset shows the low field region of all Fe doped ZnO samples, while lower inset shows M-χ_p vs H curves of $ZnFe_2O_4$.

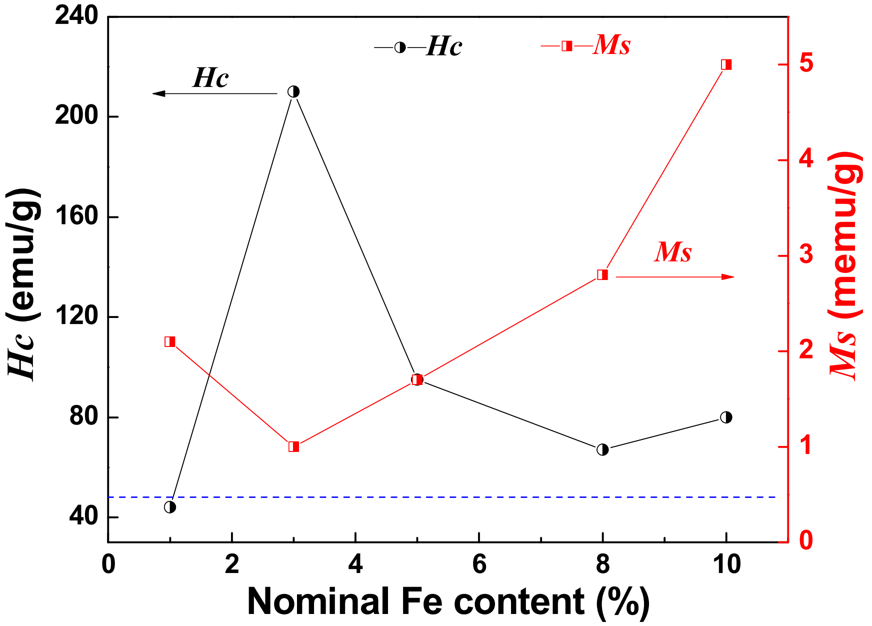

Figure 10. Variations of coercive field (Hc) and saturation magnetization (Ms) as a function of nominal Fe concentration for samples annealed at 550 °C for 1 h. The dashed line represents the Ms value of undoped ZnO.

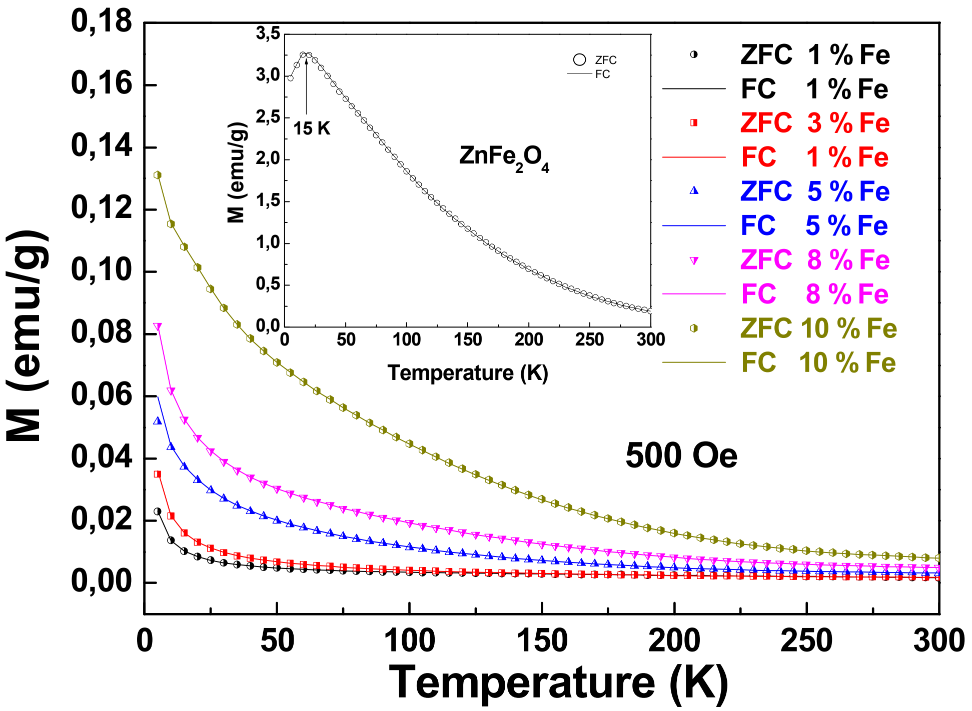

Figure 11. *M(T)* curves with H= 500 Oe for 1, 3, 5, 8 and 10 % Fe doped ZnO samples annealead for 1 h. The symbols (solid lines) correspond to ZFC (FC) data. The inset shows ZFC (FC) curves for $ZnFe_2O_4$.

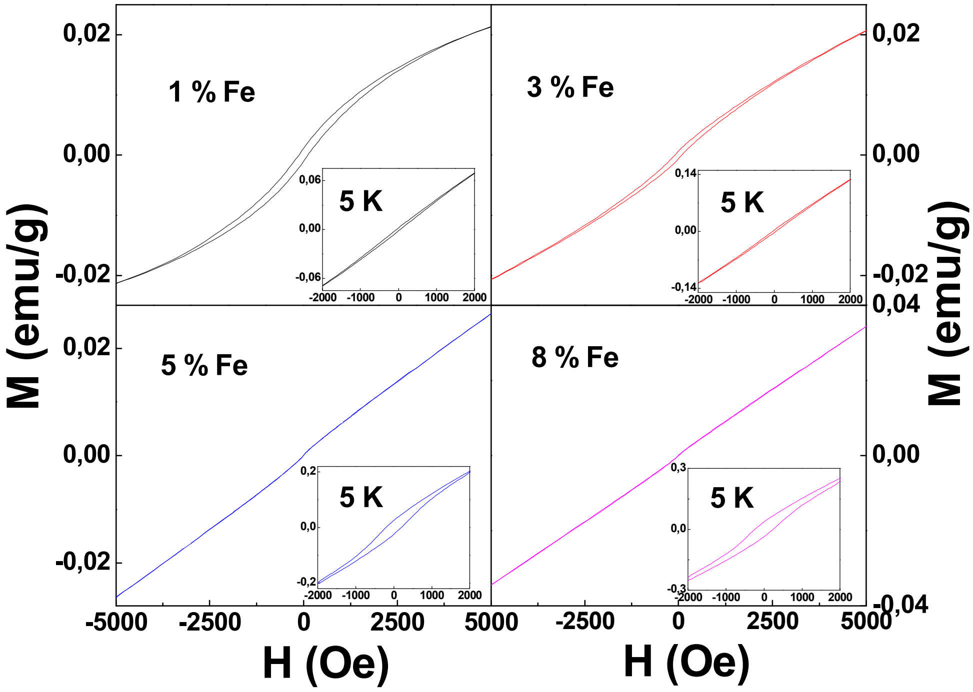

Figure 12. RT hysteresis loops for Fe doped ZnO nanoparticles along with $ZnFe_2O_4$ sample annealed for 3 h. The insets show hysteresis loops at 5 K.

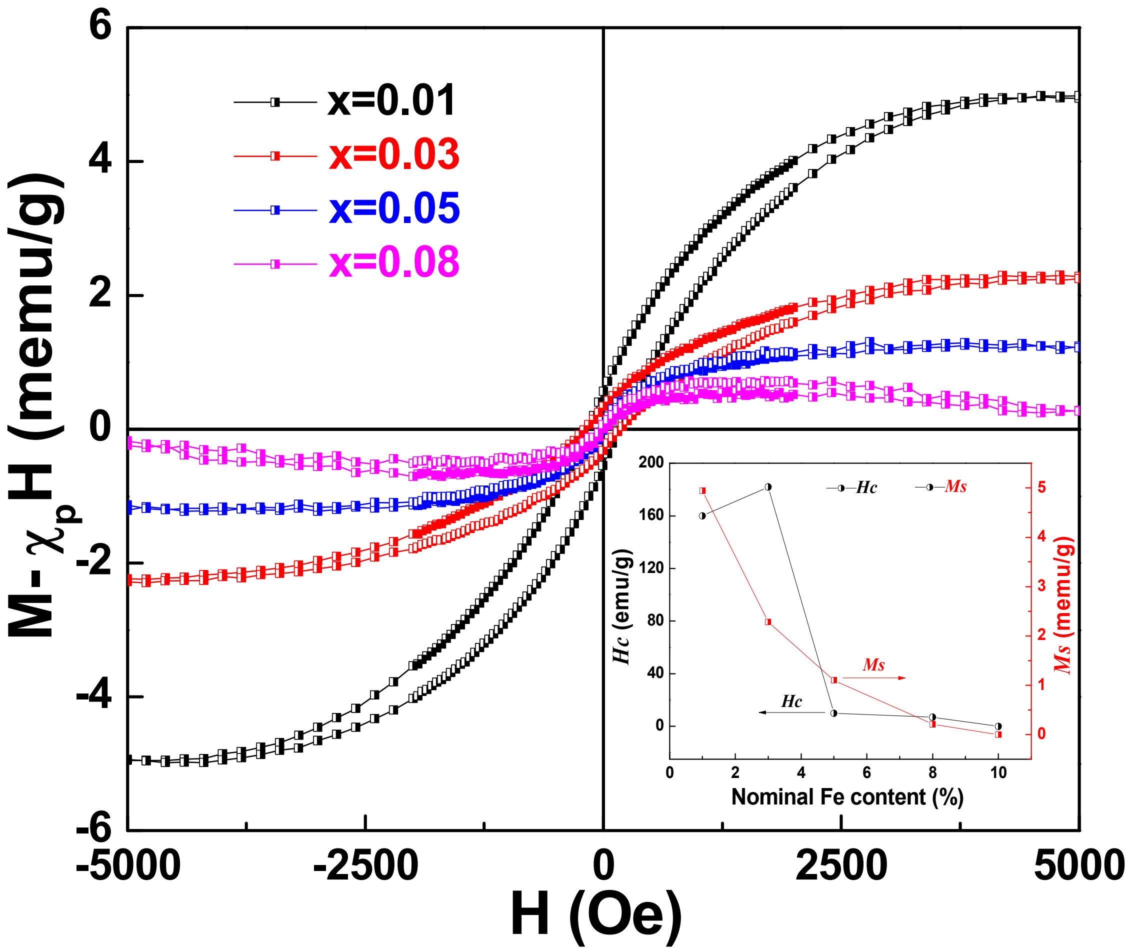

Figure 13. RT Magnetic hysteresis loops (M-χ_p vs H) of $Zn_{1-x}Fe_xO$ annealed for 3 h. The inset shows the variation of *Ms* and *Hc* with the nominal Fe content.

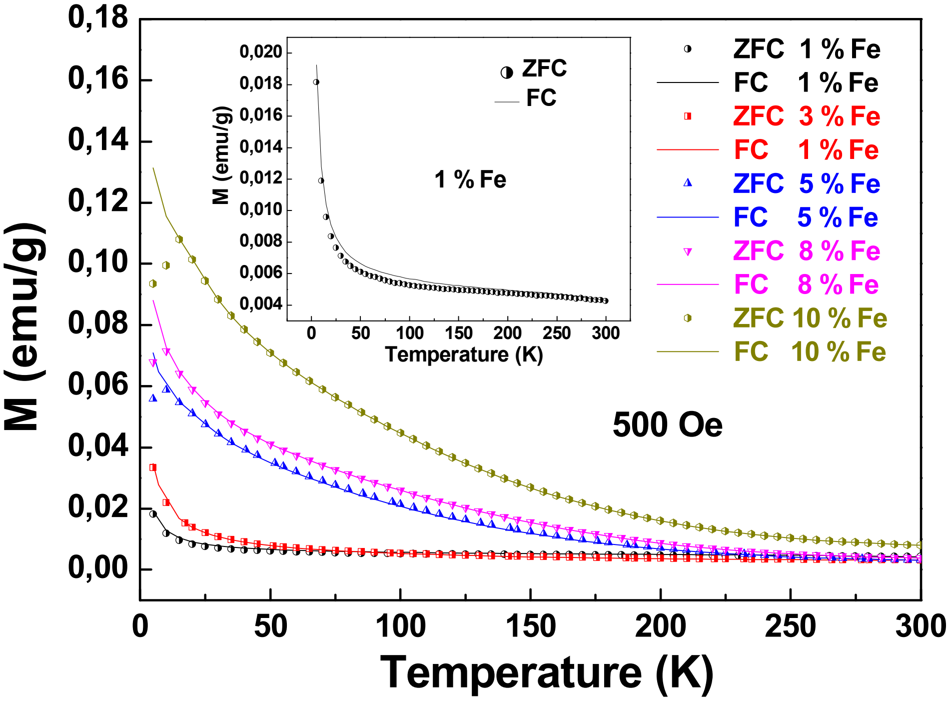

Figure 14. *M(T)* curves with H= 500 Oe for 1, 3 5, 8 and 10 % Fe doped ZnO samples annealead for 3 h. The symbols (solid lines) correspond to ZFC (FC) data. The inset shows ZFC (FC) for 1% Fe doped ZnO sample.

Graphical Abstract